PERGAMON

International Journal of Heat and Mass Transfer 42 (1999) 1405–1428

International Journal of HEAT and MASS TRANSFER

Ultra-high critical heat flux (CHF) for subcooled water flow boiling—I: CHF data and parametric effects for small diameter tubes

Issam Mudawar*, Morris B. Bowers[1]

Boiling and Two-Phase Flow Laboratory, School of Mechanical Engineering, Purdue University, West Lafayette, IN 47907, U.S.A.

Received 28 October 1997; in final form 27 July 1998

Abstract

Ultra-high critical heat flux (CHF) data, with many values exceeding 100 MW m^{-2}, were obtained using high mass velocity, subcooled water flow through short, small diameter tubes. These tests produced the highest CHF of 276 MW m^{-2} reported in the literature for a uniformly heated tube which surpassed the prior record of 228 MW m^{-2}. The data include broad ranges of tube diameter (0.406–2.54 mm), heated length-to-diameter ratio (2.4–34.1), mass velocity (5000–134 000 kg m^{-2} s^{-1}), inlet temperature (18–70°C), and outlet pressure (2.5–172.4 bars). The parametric trends of CHF were ascertained relative to all important flow and geometrical parameters. CHF increased with increasing mass velocity, increasing subcooling, decreasing tube diameter, and decreasing heated length-to-diameter ratio. For a constant inlet temperature, CHF increased with increasing pressure for pressures up to 30 bars, remained fairly constant between 30 and 150 bars, and decreased afterwards as the critical pressure was approached. CHF was accompanied by physical 'burnout' of the tube wall near the exit and tube material had little effect on the magnitude of CHF. The pressure drop for most conditions was fairly constant, albeit as high as 153.4 bars, over the entire range of heat fluxes, from the single-phase flow condition corresponding to zero heat flux up to CHF, proving that CHF was triggered even with negligible net vapor production. These high pressure drops indicate special attention should be exercised when employing the high mass velocity flows necessary to attaining ultra-high CHF. These high pressure drops also render the practice of referencing CHF data relative to a single measured pressure value very misleading.

Nomenclature

D inside tube diameter
G mass velocity
h enthalpy of fluid
h_f enthalpy of saturated liquid
h_{fg} latent heat of vaporization
k_w thermal conductivity of tube wall
L heated length of tube
L_t total length of tube
P pressure
$P_{p,i}$ pressure measured at inlet plenum
$P_{p,o}$ pressure measured at outlet plenum
ΔP measured pressure drop
ΔP_{pred} predicted pressure drop
ΔP_{SP} measured adiabatic, single-phase pressure drop
q heat flux defined using tube inside area
q_m critical heat flux (CHF) defined using tube inside area
r radial coordinate
T temperature
T_i bulk liquid temperature measured at inlet
T_o bulk liquid temperature measured at outlet
T_s reference surface temperature used in boiling curves
ΔT_{sub} liquid subcooling, $T_{sat} - T$
$\Delta T_{sub,i}$ inlet liquid subcooling based on pressure at inlet of heated length, $T_{sat,i} - T_i$
$\Delta T_{sub,o}$ outlet liquid subcooling based on inlet temperature, energy balance for entire heated length, and pressure at outlet of heated length, $T_{sat,o} - T_o$

* Corresponding author. Fax: 001 765 494 0539; e-mail: mudawar@ecu.purdue.edu

[1] Former graduate student; current address: Motorola, Cellular Infrastructure Group, 1475 West Shure Drive, Arlington Heights, IL 60004, U.S.A.

0017–9310/98/$ - see front matter
PII: S0017–9310(98)00241–5

T_{sat} saturation temperature
t_w tube wall thickness
x thermodynamic equilibrium quality, $(h-h_f)/h_{fg}$
x_i thermodynamic equilibrium quality based on pressure at inlet of heated length, $(h_i-h_{f,i})/h_{fg,i}$
x_o thermodynamic equilibrium quality determined from x_i, energy balance for entire heated length, and pressure at outlet of heated length, $(h_o-h_{f,o})/h_{fg,o}$.

Subscripts
c upstream contraction
e downstream expansion
f friction
i inlet of heated length
o outlet of heated length.

1. Introduction

Critical heat flux (CHF) refers to the heat transfer limit causing a sudden decrease in the heat transfer coefficient and possible catastrophic failure of a device in which evaporation or boiling is occurring. The high heat dissipation rates (about 1 MW m^{-2}) required in the electronics industry (e.g., supercomputers, power devices, military avionics modules) can be achieved without exceeding CHF by using relatively low mass velocity, flow boiling of dielectric coolants in small diameter channels [1–3]. On the other hand, cooling of devices such as high-power lasers, rocket nozzles, fusion reactor components, and particle accelerator targets necessitate what can be referred to as ultra-high heat flux cooling technologies. The heat flux requirements in these devices are typically over 25 MW m^{-2}, far greater than those of electronic cooling. Heat loads for fusion reactor components, for example, require dissipation of heat fluxes on the order of 100 MW m^{-2} [4]. Since these heat fluxes exceed the CHF attainable with common flow boiling systems, the ability to both greatly increase and predict the magnitude of CHF is of paramount importance to ultra-high heat flux applications. High mass velocity, subcooled flow boiling of water is required to insure that the extreme operating conditions in these applications maintain heat fluxes in the nucleate boiling regime safely below CHF. Low cost, availability and high latent heat of vaporization render water the ideal coolant under these conditions.

Low and high mass velocity flows are characterized by drastically different flow patterns as well as unique CHF trigger mechanisms. Shown on the left-hand side of Fig. 1 is a subcooled liquid entering a uniformly heated tube at low mass velocity. The combination of low mass velocity and a long tube often results in a near saturated vapor flow at the tube exit. In the entrance region, heat is transferred to the fluid by single-phase forced convection and the bulk temperature rises as a result of sensible energy exchange. As the bulk temperature rises so does the wall surface temperature. The wall temperature eventually becomes sufficiently higher than the liquid saturation temperature allowing sustained bubble growth and signaling the onset of subcooled nucleate boiling. Subcooled boiling refers to the region where the thermodynamic equilibrium quality, averaged over the tube cross-sectional area, is less than zero. The flow assumes a 'bubbly flow' pattern with bubbles emanating from the surface being swept along. The core temperature continues to rise due to latent heat exchange as bubbles pulled into the subcooled core condense. Progressing along the tube, the flow eventually attains a thermodynamic equilibrium quality of zero which defines the beginning of the saturated nucleate boiling region. The liquid core in this region, however, remains slightly subcooled and a bubbly flow pattern persists. Once the liquid core temperature reaches the saturation temperature, vapor bubbles no longer condense and, instead, they grow and coalesce creating a 'slug flow' or 'churn flow' pattern. Vapor continues to accumulate until bubble coalescence in the central core becomes sufficient to establish a continuous vapor core. The liquid exists primarily as a thin film along the tube wall in this 'annular-flow' regime. A fine mist of liquid droplets, which were created by the break-up of liquid bridges between large vapor bubbles in the upstream, slug or church flow regimes, is transported within the vapor core. Boiling continues to occur along the surface covered by the liquid film until the film becomes too thin to sustain bubble nucleation and forced convection heat transfer to the film, along with interfacial evaporation, ensues. Eventually, the film dries out due to complete liquid evaporation or the liquid film flow rate approaching zero as a result of momentum losses. Liquid film dryout is the mechanism responsible for the relatively low CHF values associated with saturated boiling in long tubes with low inlet subcooling.

High mass velocity flow in a short tube with high inlet subcooling results in subcooled boiling and higher CHF values as illustrated by the tube on the right-hand side of Fig. 1. Like the previous case, the flow is characterized by an inlet region of single-phase convection until the onset of nucleate boiling. Once nucleation begins, very small bubbles are formed creating a thin bubble boundary layer, and bubbles migrating toward the core quickly condense. The core temperature rises as a result of the energy transfer; however, the flow remains in the subcooled boiling region over its entire heated length. CHF can occur while the thermodynamic equilibrium quality is well below zero and is commonly referred to as departure from nucleate boiling (DNB). For high-flux DNB, the term 'burnout heat flux' is also used because physical destruction of the system will occur as a result of a large wall temperature excursion. The mechanism for subcooled CHF or 'burnout' is not well understood, though several theories exist: intense boiling causes the bubble–

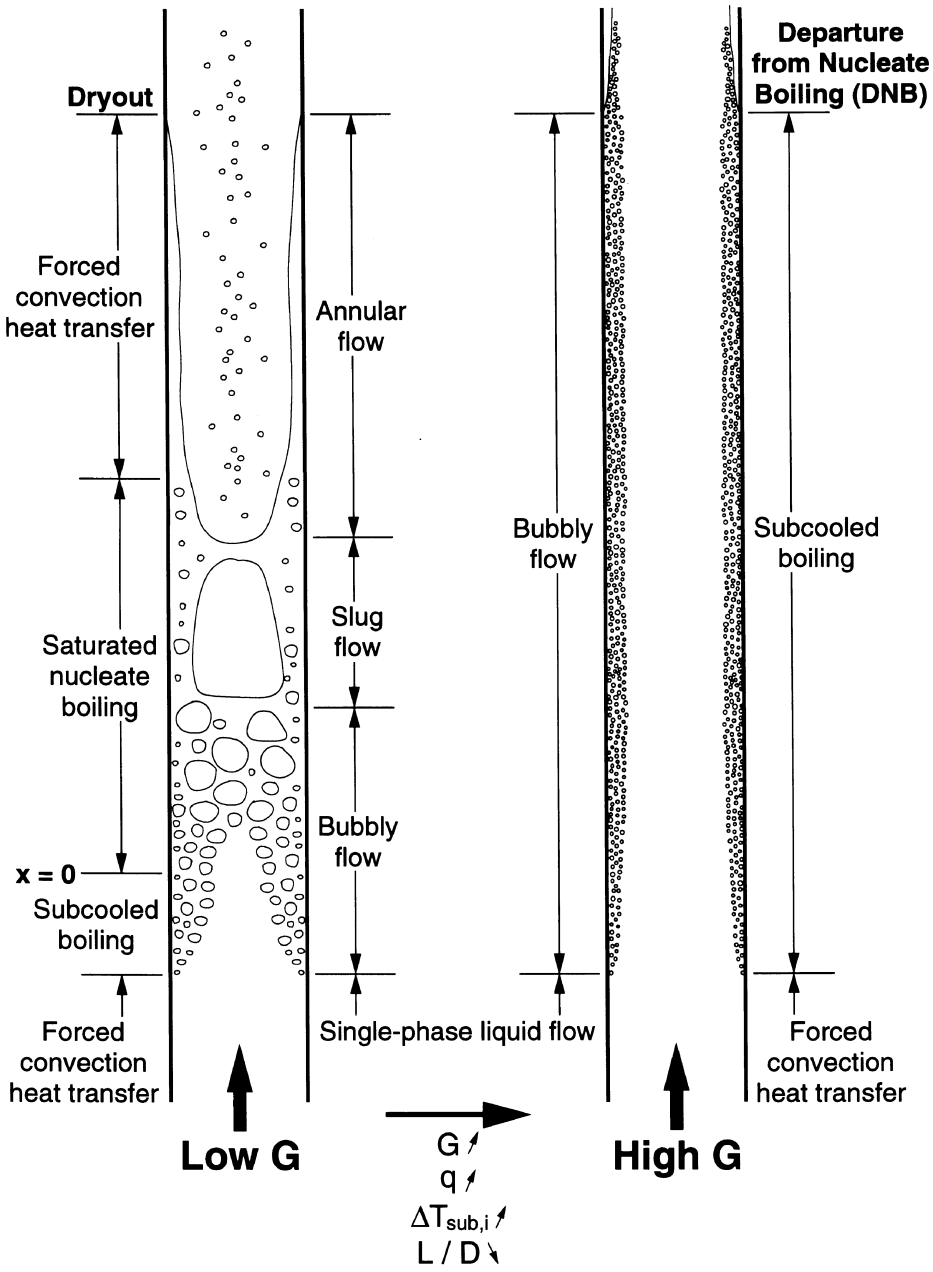

Fig. 1. Heat transfer regions and flow patterns in a uniformly heated tube for conditions of low and high mass velocity flows.

liquid boundary layer to separate from the heated wall and the resulting stagnant liquid to evaporate [5], bubble crowding within the boundary layer inhibits liquid replenishment near the surface causing the formation of a vapor layer [6], and dryout of a liquid sublayer beneath a large vapor bubble causes local wall temperature to rise [7].

Previous studies have shown that CHF in any two-phase cooling configuration generally depends upon key parameters which include working fluid, geometry, mass velocity, subcooling, and pressure. Only a few studies have been published on the ultra-high CHF regime. These studies have shown ultra-high CHF can be achieved with subcooled flow boiling of water at high mass velocities in small diameter tubes. Ornatskii and Vinyarskii [8] reported an appreciable rise in ultra-high CHF with increased exit subcooling for water flow in tubes with $D = 0.4$–2 mm. Similar trends have been reported for

water flow by Celata et al. [9] for $D = 2.5$ mm and Vandervort et al. [10] for $D = 0.33$–2.67 mm. Increasing mass velocity has also been reported to yield monotonic increases in ultra-high CHF [8–12].

The reported influences of tube geometry and pressure are less consistent than those of subcooling and mass velocity. With regards to the tube length and diameter effects on CHF, Bergles [13] observed an increase in CHF with decreasing heated length and decreasing tube diameter. Vandervort et al. also measured an increase in CHF with decreasing L/D, especially for $L/D < 10$. Vandervort et al. also concluded the diameter effect is most pronounced at high mass velocities, which contradicts Ornatskii and Vinyarskii's observation of a diminution in the diameter effect for large mass velocities.

The effect of pressure on CHF is even more complicated than those of the other parameters just mentioned. Bergles reported an increase in CHF with increasing pressure for pressures between 1.38 and 5.86 bars. On the other hand, Ornatskii and Vinyarskii measured an increase in CHF with decreasing outlet pressure, and Vandervort et al. found no significant outlet pressure effect on CHF for pressures below 25 bars.

A comprehensive review of prior ultra-high CHF work by the present authors has revealed that much of the inconsistencies between the findings of different investigators can be traced to one or more of the following: (1) inability to isolate the effects of key parameters while keeping all others constant, (2) very few short heated length-to-diameter ratio data, (3) inability to attain very high mass velocities (no data exist for mass velocities over 90 000 kg m^{-2} s^{-1}), and (4) inability to cover a broad range of pressures, especially for high mass velocities. While gaps in the data from previous studies can be the result of poor isolation of parametric effects by individual investigators, most are actually due to limitations of the experimental apparatus used (e.g., limited pump pressure and/or flow rate capability, power supply limitations, test section construction). In addition, little attention has been given to predicting or measuring the enormous pressure drop resulting from the high mass velocities ultra-high CHF often demands. This pressure drop renders the practice of referencing CHF data relative to a single measured pressure value very misleading.

In the present study, an experimental facility was designed to overcome the aforementioned limitations of prior ultra-high CHF work. In the present Part I of a two part study, the results of an extensive experimental investigation of ultra-high CHF for water flow in small diameter tubes of short heated length are presented. The present CHF data are included in Part I along with a discussion of the effects of mass velocity, heated length, tube diameter, pressure, and subcooling on CHF. Part II [14] complements this study with the development of (1) a pressure drop model for predicting the pressure drops associated with high mass velocity flows required for attaining ultra-high CHF, and (2) design correlations for accurate prediction of ultra-high CHF.

2. Experimental facility

2.1. Flow loop

The present study demanded a flow loop capable of withstanding pressures nearing the critical point. As shown in Fig. 2, water was fed from a large reservoir to a high pressure piston pump which both increased the pressure and circulated the fluid through the loop. Submerged inside the reservoir were both a cooling coil and an immersion heater. These were used to heat or cool the reservoir water, thereby providing a means for controlling the test section's inlet temperature. The high pressure pump consisted of three pistons operating out of phase to deliver a steady 15.1 liter min^{-1} (4 gpm) stream of water at a maximum pressure of 206.8 bars (3000 psi). Located immediately at the pump exit was an unloader valve, a device which protected the pump by forcing the flow to a recirculating loop in the event of an excessive increase in flow resistance downstream. Leaving the unloader valve, the fluid entered a pulsation dampener that reduced fluctuations in both flow rate and pressure. A portion of the flow then entered the test section while the balance returned to the reservoir through a by-pass. A separate flow loop also shown in Fig. 2 was utilized for deaeration of the water prior to conducting a series of tests.

The flow rate as well as the outlet pressure were controlled by valves located in the test section line and the by-pass. A turbine flow meter used to measure the flow rate was located upstream of the test section. Both inlet and outlet pressures were measured using pressure gauges; however, for pressure drops below 3.45 bars (50 psi), a differential pressure transducer was used to acquire more accurate readings of the pressure drop.

2.2. Test section

The test section shown in Fig. 3 consisted of inlet and outlet power/instrumentation blocks that were identical in construction and designed for convenient connection to the test section using compression fittings. To maintain correct spacing between the blocks as well as provide support for the test section, the two blocks were fastened to a stainless steel support bar that included a track on the lower end for attaching the inlet block. Each block was fabricated from two stainless steel plates separated by a thick plate of G-7 fiberglass plastic. The plastic insulated the stainless steel plates from each other both electrically and thermally. A 6.35 mm (0.25 in.) diameter hole was drilled through the stainless steel and G-7 plates

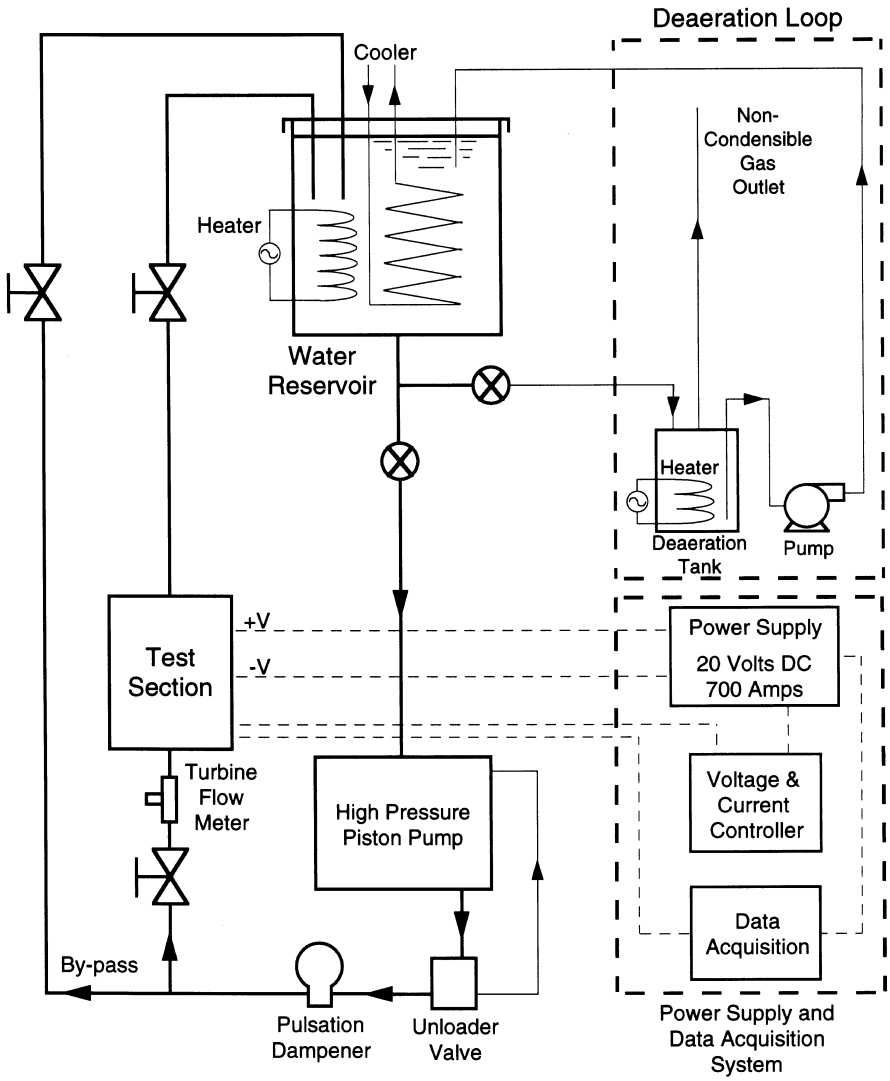

Fig. 2. Schematic of flow loop.

and served as a fluid flow path to and from the test section. One stainless steel plate in each block served as an electrode which provided a resistance free path for electrical current from the power lead to the test section. It included a threaded connection so that a standard compression fitting could be used for connecting the electrode and the copper support of the test section. The other stainless steel plate in each block was machined with two ports in addition to a threaded connection for attaching a compression fitting for the water inlet or outlet. One of the ports was used for pressure measurement, the other for a temperature probe. To provide an appropriate high pressure seal, 0-rings were used between each stainless steel plate and the insulating plastic plate, and the three plates were clamped together with four steel bolts. In order to maintain electrical and thermal isolation between the bolts and electrode, G-7 sleeves separated the two metal plates where the bolts passed through the electrode, and a G-7 gasket provided electrical insulation between the bolt heads and the electrode.

The detail in Fig. 3 shows an AISI stainless steel 304 (or Cu–Ni 30%) capillary tube silver soldered to copper support pieces at each end. The solder joint provided a seal between the capillary tube and copper supports pieces that could withstand both high pressures and high temperatures as well as maintain very low electrical resistance. Each of the two 6.35 mm o.d. copper supports had a 2.84 mm i.d. hole through its center. The support pieces provided a convenient method of joining the test section to the electrodes using brass compression fittings.

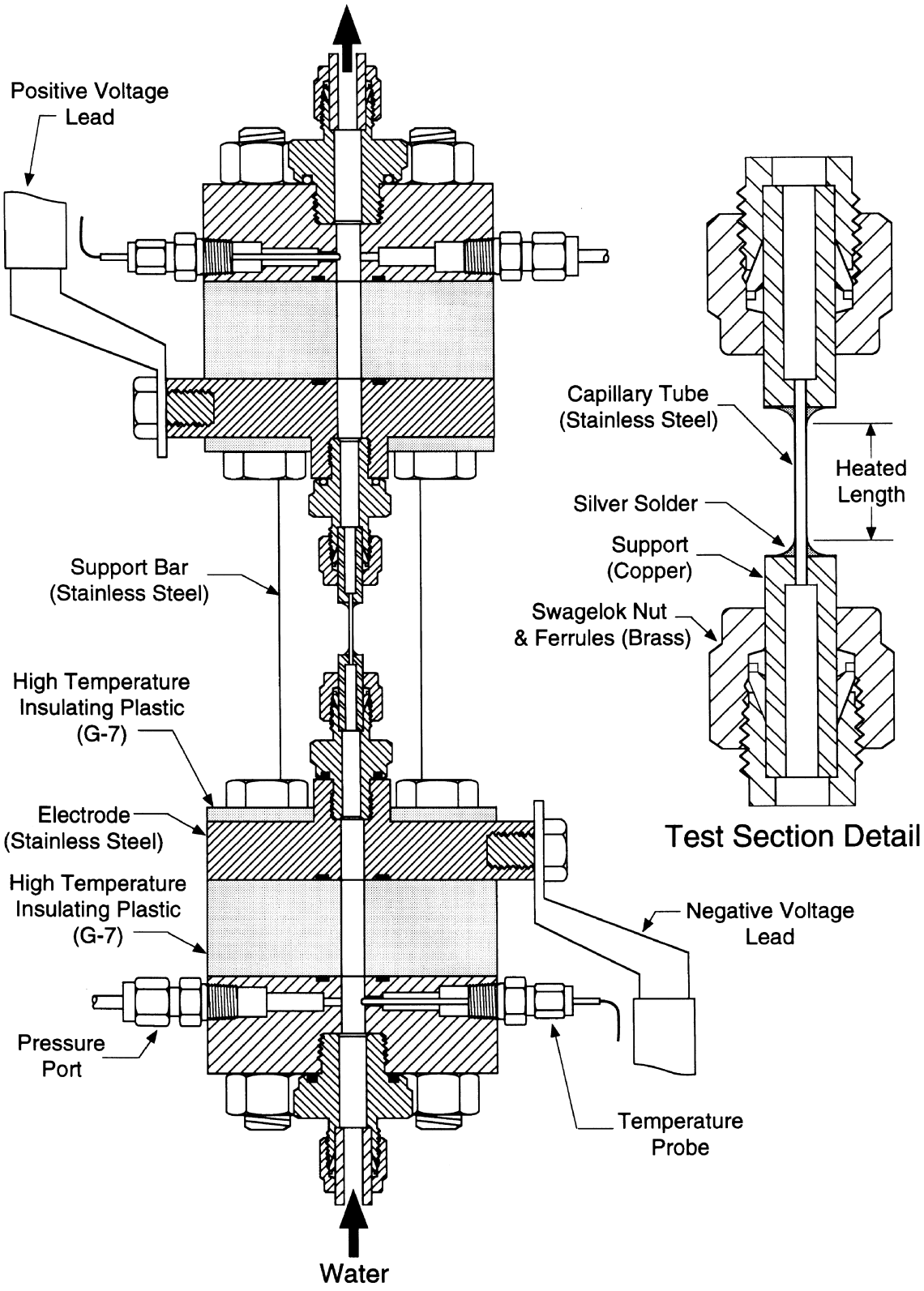

Fig. 3. Schematic of test section.

2.3. Data acquisition and measurement uncertainty

Power cables from a d.c. power supply were connected to the two stainless steel plates mounted to the tube ends. Heat was generated in the capillary tube by passing an electrical current (up to 700 amperes and 20 volts) from one stainless steel plate through the tube itself and returning to the power supply from the other stainless steel plate. The electrical resistance of the capillary tube wall was much greater than the remainder of the electrical path (power cables, stainless steel electrodes, brass compression fittings, copper support pieces, and solder joints); Bowers [15] experimentally demonstrated that over 97% of the supplied electrical power was dissipated uniformly along the inner surface of the tube.

Critical heat flux tests were conducted for different combinations of flow parameters such as flow rate, inlet temperature, and outlet pressure. While performing a given test, these parameters were continuously monitored, and the heat flux, calculated from power measurements and heat dissipation area (inner surface area of tube between solder joints), was increased in very small increments. Power delivered to the test section was determined from the product of current through and voltage across the test section. Following each power increment, steady state was achieved and additional flow adjustments were made in order to maintain the appropriate test conditions. CHF values were very high resulting in physical 'burnout' of the capillary tube. Thus, the criterion used for determining CHF was the tube 'burnout'.

Compared with the heat dissipated to the water flowing within the test section, heat losses from natural convection and radiation were less than 0.2%, and from axial heat conduction 1.0% (see ref. [15]). Since only an upper limit could be ascertained for heat losses and these losses were smaller than 1.2% of the electrical power dissipated in the tube, all CHF values reported in this paper were based on electrical power divided by the inner surface area of the tube between the solder fronts. Uncertainties in both current and voltage resulted in an uncertainty in power measurement of less than 3.0%. The tube inside diameter proved to be within the 6.3 and 4.2% uncertainty specified by the manufacturer for the 0.406 and 0.902 mm tubes (bulk of present data), respectively. The heated length was measured using a micrometer in conjunction with a microscope resulting in an uncertainty of less than 2.0%. Voltage and current were recorded every 2 s and the mean value and standard deviation of the heat flux were determined over 30-s intervals. The standard deviation quantified the small fluctuations in heat flux under steady state conditions. This additional uncertainty in heat flux was at most 2.0 and 1.5% for the 0.406 and 0.902 mm tubes, respectively. Combining this uncertainty with the geometrical and power measurement uncertainties resulted in a total uncertainty in the heat flux measurement of less than 8.0% and 6.0% for the 0.406 and 0.902 mm tubes, respectively [15].

3. Experimental investigation

3.1. Test conditions

Ultra-high CHF demands very high mass velocity flow of subcooled water through short, small diameter tubes at somewhat elevated pressures. Because of experimental difficulties, ultra-high CHF data (above 100 MW m^{-2}) are very limited. The present investigation incorporated a facility which overcame many of the difficulties encountered by prior investigators in obtaining such data. The unique attributes of this facility enabled testing at pressures approaching the critical point, reaching very high mass velocities, and accommodating the high pressure drops associated with high mass velocity flow through small diameter tubes. The present study also included very short heated lengths because previous studies have shown decreasing heated length can greatly ameliorate CHF. Aside from attempting to fill a data gap in the CHF literature, specific tests were performed to build a broad range of ultra-high CHF data which addresses the parametric effects of mass velocity, heated length, tube diameter, pressure, and subcooling on CHF.

For ultra-high heat fluxes, CHF is synonymous with the burnout heat flux because achieving CHF causes system destruction or meltdown as a result of the large temperature excursion that accompanies the large reduction in the heat transfer coefficient. The photograph of a test section ($D = 0.902$ mm) after burnout in Fig. 4 clearly illustrates this method of detecting CHF for ultra-high heat fluxes. A well-defined cut in the tube is visible where the tube wall literally melted along a circumferential section perpendicular to the flow and burst open upon the occurrence of CHF. This cut was initiated with a single glowing hot spot which spread circumferentially prior to CHF. The location of burnout is near the tube exit which was characteristic of all the cases tested. It should be emphasized that all mechanical loads in the test tube were maintained safely below the yield strength of the tube material at the highest temperature prior to CHF. This precluded the occurrence of stress-induced, low-temperature fracture and provided the needed confidence in the CHF detection method.

The complete data of the present study are presented in Table 1. Outlet quality and subcooling were calculated from outlet enthalpy which was determined using an energy balance,

$$h_o = h_i + 4\frac{Lq_m}{DG}.$$

Thermophysical properties required by these parameters were evaluated at the outlet pressure which was determined using the pressure drop model from Part II of the present study [14]. The bulk of the data was obtained for tube diameters of 0.406 and 0.902 mm and a heated length of about 5.6 mm; however, additional tests were

Fig. 4. AISI type 304 stainless steel test section ($D = 0.902$ mm, $t_w = 0.089$ mm, $L/D = 6.4$) following burnout.

performed with tube diameters of 0.500, 0.635, 1.07, and 2.54 mm and heated lengths up to 30.8 mm. The present study covered very broad ranges of mass velocity ($G = 5000$ to 134 000 kg m^{-2} s^{-1}) and pressure ($P_o = 2.5$ to 172.4 bars). Figure 5 shows in a mass velocity–pressure plane the present ultra-high CHF study containing a much greater number of high mass velocity and high pressure/high mass velocity data than the prior ultra-high CHF studies. The corresponding CHF values ranged from 9.4 to 276 MW m^{-2}, the upper limit being the highest CHF ever reported in the literature for a uniformly heated tube. This value surpasses the prior CHF record of 228 MW m^{-2} achieved by Ornatskii and Vinyarskii [8].

3.2. Boiling curve

A few qualitative boiling curves were obtained to provide a better understanding of two-phase heat transfer for high mass velocity flow in small diameter tubes. Figure 6 shows boiling curves for a tube with an internal diameter of 0.902 mm at mass velocities of 15 000 and 30 000 kg m^{-2}s^{-1}. The heated length for these cases was 5.8 to 5.9 mm. The temperature difference presented along the abscissa is the inner surface temperature, T_s, minus the inlet temperature, T_i. The inner surface temperature was obtained by correcting the measured outer surface temperature for the temperature gradient across the tube wall. A specially designed thermocouple clip was used for measuring the outer surface temperature. A thermocouple was embedded within boron nitride (ceramic with high electrical resistivity and high thermal conductivity) which was in direct contact with the tube's outer surface. The thermocouple clip, which covered a 2 mm segment of the outer tube surface, was located halfway along the tube length. This was approximately 36% of the overall heated length; therefore, the measured surface temperature, T_s, represents an average inner surface temperature rather than the precise surface temperature at a specific axial location.

Figure 6 shows a well defined single-phase region characterized by a fairly constant 45° slope for low heat fluxes up to the point where the slope begins to increase with increasing heat flux following the onset of nucleate boiling. Within the single-phase region, there is a distinct offset between the two curves, with the high mass velocity curve producing a lower temperature difference for the same heat flux due to a higher heat transfer coefficient. The two curves approach each other within the nucleate boiling regime, culminating in a CHF of 51.0 MW m^{-2} for $G = 15\,000$ kg m^{-2} s^{-1} and a 90% greater CHF when the mass velocity is doubled.

Aside from illustrating general boiling trends, the boiling curves in Fig. 6 demonstrate the existence of a well defined nucleate boiling regime prior to CHF. While this may appear to be a straight-forward conclusion for any boiling study, high mass velocity CHF is quite unique in that, quite often, little change occurs in the key flow parameters of interest, such as pressure drop, as heat flux is increased to CHF. Furthermore, bubbles in a high mass velocity flow are very small and tend to condense very rapidly upon departure from the tube wall. Consequently, there has been concern that burnout may actually occur directly from the single-phase flow regime. Obviously, Fig. 6 proves otherwise.

The tubes used throughout this study were thin-walled to provide sufficient electrical resistance for generating the required high heat fluxes. However, associated with the high rate of heat generation was a large temperature gradient across the tube wall. As an example, Fig. 7(a) compares the temperature distributions across the tube

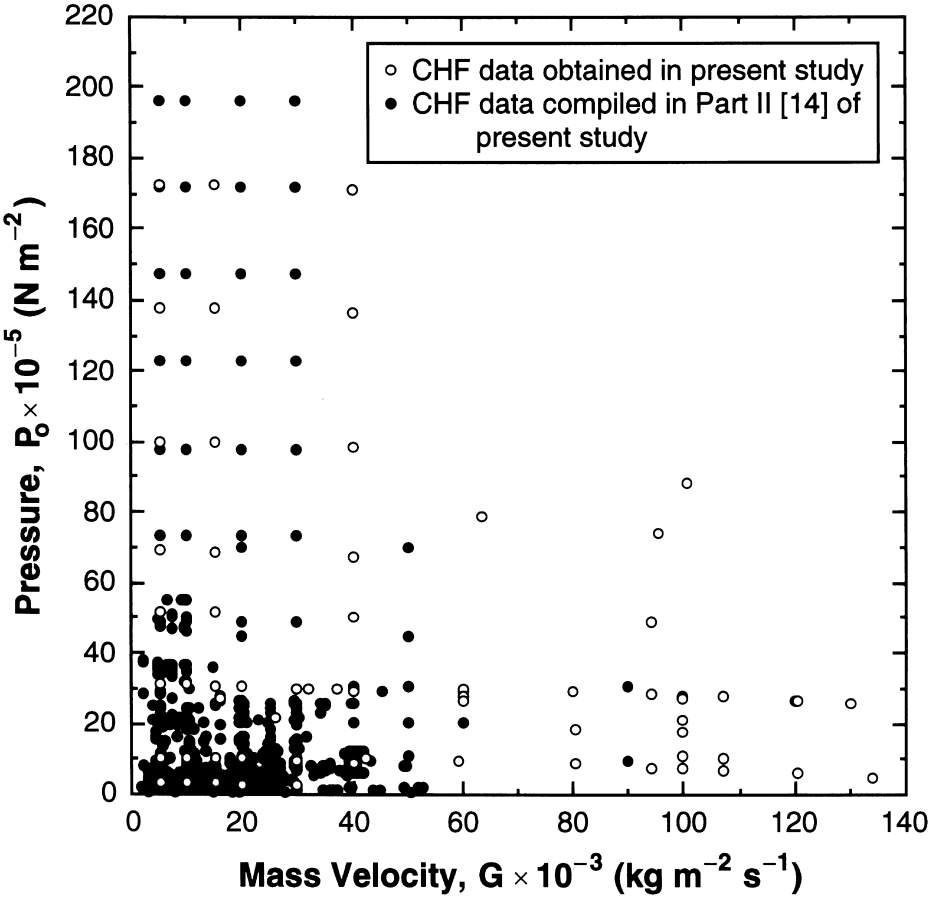

Fig. 5. Subcooled high-CHF data in the mass velocity–pressure plane.

wall for an ultra-high heat flux of 300 MW m^{-2} and a moderately high heat flux of 30 MW m^{-2}. The temperature distribution was calculated from an analytical one-dimensional heat diffusion model, assuming uniform heat generation in a cylindrical cross section with an adiabatic outer boundary (i.e., neglecting natural convection and radiation effects on the tube exterior) and a known inner surface temperature. The inner temperature was set equal to the saturation temperature of water at 31.0 bars which corresponds to a large fraction of the present data. As illustrated, the higher heat flux creates a temperature difference between the inner and outer surfaces of approximately 500 and 400°C for the 0.902 and 0.406 mm tubes, respectively. Even though the gradient is very large, the outer surface temperature remains over 600°C below the melting point for 304 stainless steel. This shows that determining CHF by tube burnout is a valid technique, since the tube would burst only as a result of a sudden large increase in the inner surface temperature.

Figure 7(b) compares the wall temperature gradient for 304 stainless steel ($k_w = 22$ W m^{-1} K^{-1}) and Cu–Ni 30% ($k_w = 38$ W m^{-1} K^{-1}) tubes of similar diameter. The wall thickness for the latter tube is approximately 63% greater than the stainless steel tube; however, the thermal conductivity of the copper alloy is more than twice that of stainless steel. The net result is a lower temperature difference between the inner and outer surfaces for the Cu–Ni 30% tube. The melting point for Cu–Ni 30% is also lower; however, the surface temperature remains more than 500 °C below the melting point.

It can be concluded from Fig. 7(a) and (b) that even at the highest heat flux achieved in the present study, 276 MW m^{-2}, the tube outer surface was well below the melting point until CHF occurred. Thus, the technique used for detecting CHF did not yield results that were dependent upon the tube wall material. Figure 8 further supports this conclusion by comparing CHF over a broad range of mass velocity ($G = 20\,000$ to $100\,000$ kg m^{-2} s^{-1}) for tubes of different wall materials but similar dimensions. The CHF data for both materials show a close resemblance and good repeatability.

Table 1
CHF and pressure-drop data for vertical upflow of water in a uniformly heated round tube

Test no.	L (mm)	L/D	$G\times10^{-3}$ (kg m^{-2} s^{-1})	$P_{p,o}$ (bars)	$\Delta P = P_{p,i} - P_{p,o}$ (bars)	$\Delta P/\Delta P_{SP}$ (bars)	T_i (°C)	T_o (°C)	$q_m\times10^{-6}$ (W m^{-2})	ΔP_c (bars)	ΔP_f (bars)	ΔP_e (bars)	ΔP_{pred} (bars)	P_i (bars)	P_o (bars)	$\Delta T_{sub,i}$ (°C)	x_i	$\Delta T_{sub,o}$ (°C)	x_o
$D = 0.406$ mm, $t_w = 0.077$ mm, material: AISI SS–304																			
1	6.0	14.8	20.0	31.0	12.1	0.95	24	62	95.0	3.0	2.7	−0.1	5.6	33.7	30.9	216	−0.532	144	−0.355
2	10.8	26.6	25.8	22.1	9.0	0.93	27	73	75.0	4.9	5.7	−0.1	10.5	27.8	21.9	202	−0.482	116	−0.271
3	5.6	13.8	40.0	31.0	19.3	1.08	25	56	125.0	11.8	8.5	−0.3	19.9	39.4	30.4	224	−0.569	169	−0.410
4	5.3	13.1	40.0	31.0	-	-	24	55	131.0	11.8	8.6	−0.3	20.0	39.5	30.4	225	−0.572	170	−0.413
5	5.6	13.8	40.0	31.0	18.6	1.04	24	56	125.0	11.8	8.6	−0.3	20.0	39.5	30.4	225	−0.572	170	−0.412
6	5.8	14.3	40.0	31.0	19.3	0.95	25	57	122.0	11.8	8.5	−0.3	19.9	39.4	30.5	224	−0.569	168	−0.409
7	6.3	15.5	40.0	31.0	19.3	0.97	25	60	121.0	11.8	8.5	−0.3	19.9	39.4	30.5	224	−0.569	165	−0.402
8	9.0	22.2	42.3	10.3	20.7	0.94	25	73	109.0	13.2	9.3	−0.4	22.1	19.3	9.9	186	−0.420	100	−0.212
9	10.5	25.9	59.0	10.3	42.8	0.90	30	75	114.0	25.5	22.2	−0.7	47.1	32.2	9.2	208	−0.507	99	−0.208
10	5.0	12.3	60.0	31.0	36.9	0.96	25	53	170.0	26.4	16.7	−0.7	42.4	47.5	29.8	235	−0.623	175	−0.424
11	5.7	14.0	60.0	31.0	41.4	0.95	25	58	165.0	26.4	16.7	−0.7	42.4	47.4	29.8	235	−0.623	172	−0.416
12	6.3	15.5	60.0	31.0	44.8	1.07	25	62	190.0	26.4	16.7	−0.7	42.4	47.4	29.9	235	−0.622	162	−0.393
13	4.9	12.1	80.0	31.0	77.6	1.07	25	56	235.0	46.8	27.0	−1.3	72.5	57.5	28.9	248	−0.689	173	−0.416
14	6.1	15.0	80.0	31.0	82.8	0.94	25	61	221.0	46.8	27.0	−1.3	72.5	57.4	29.1	247	−0.688	168	−0.404
15	9.3	22.9	80.4	20.7	70.3	0.94	36	85	168.0	47.3	35.8	−1.3	81.8	56.0	18.6	235	−0.650	127	−0.288
16	8.2	20.2	80.4	10.3	65.5	0.90	34	73	160.0	47.3	25.6	−1.3	71.6	34.9	8.7	208	−0.516	102	−0.212
17	5.4	13.3	94.1	10.3	82.1	0.99	23	46	177.0	64.6	35.9	−1.8	98.7	45.4	7.5	235	−0.614	121	−0.250
18	5.8	14.3	94.1	31.0	86.2	1.00	23	52	198.0	64.6	35.9	−1.8	98.7	66.0	28.3	259	−0.752	179	−0.429
19	5.5	13.5	94.1	51.7	84.5	0.92	25	51	190.0	64.6	35.4	−1.8	98.2	86.2	48.9	275	−0.888	211	−0.566
20	6.1	15.0	100.0	10.3	120.6	0.97	25	55	219.0	73.0	39.2	−2.0	110.1	48.4	7.3	237	−0.629	111	−0.228
21	5.3	13.1	100.0	13.8	129.3	0.97	25	55	233.0	73.0	39.2	−2.0	110.1	52.1	10.7	241	−0.653	129	−0.274
22	5.9	14.5	100.0	13.8	110.3	0.94	26	62	270.0	73.0	38.9	−2.0	109.9	51.7	10.8	240	−0.648	120	−0.256
23	5.7	14.0	100.0	20.7	113.7	0.97	26	57	237.0	73.0	38.9	−2.0	109.9	58.6	17.7	248	−0.694	149	−0.333
24	5.6	13.8	100.0	20.7	106.9	0.94	25	56	220.0	73.0	39.2	−2.0	110.1	58.9	17.6	249	−0.699	152	−0.341
25	5.7	14.0	100.0	20.7	94.8	0.95	25	56	250.0	73.0	39.2	−2.0	110.1	58.9	17.7	249	−0.698	148	−0.332
26	5.8	14.3	100.0	31.0	108.9	0.99	25	53	215.0	73.0	39.2	−2.0	110.1	69.2	28.0	260	−0.767	176	−0.420
27	5.8	14.3	100.0	31.0	93.1	0.96	25	61	274.0	73.0	39.2	−2.0	110.1	69.2	28.0	260	−0.767	168	−0.402
28	5.8	14.3	100.0	31.0	102.4	0.96	26	62	270.0	73.0	38.9	−2.0	109.9	68.9	28.0	259	−0.762	167	−0.401
29	5.3	13.1	100.0	31.0	87.9	0.94	25	55	252.0	73.0	39.2	−2.0	110.1	69.3	27.9	260	−0.768	173	−0.415
30	6.1	15.0	100.0	31.0	104.8	0.98	26	62	259.0	73.0	38.9	−2.0	109.9	68.8	28.0	259	−0.762	167	−0.401
31	4.5	11.1	107.2	10.3	104.4	0.99	23	34	109.0	83.8	44.7	−2.3	126.1	54.1	6.5	246	−0.672	128	−0.262
32	4.6	11.3	107.2	10.3	108.6	0.97	26	42	142.0	83.8	43.7	−2.3	125.2	53.1	6.6	241	−0.657	122	−0.249
33	6.0	14.8	107.2	10.3	111.0	0.98	25	47	158.8	83.8	44.0	−2.3	125.5	53.1	6.9	242	−0.660	119	−0.243
34	5.8	14.3	107.2	10.3	108.6	0.93	24	52	208.0	83.8	44.3	−2.3	125.8	53.4	6.8	244	−0.665	114	−0.233
35	8.5	20.9	107.2	13.1	99.0	0.88	40	83	215.0	84.0	39.9	−2.3	121.5	51.1	10.3	225	−0.608	101	−0.215
36	6.0	14.8	107.2	31.0	106.9	1.00	25	53	206.0	83.8	44.0	−2.3	125.5	73.8	27.6	264	−0.799	177	−0.423
37	5.8	14.3	120.0	31.0	129.3	0.88	27	61	276.0	104.9	52.4	−2.9	154.4	81.8	26.7	270	−0.849	169	−0.402
38	5.8	14.3	120.0	31.0	122.4	0.91	26	56	247.0	104.9	52.7	−2.9	154.8	82.2	26.7	271	−0.855	174	−0.412
39	5.1	12.6	120.4	10.3	143.4	0.92	25	46	165.8	105.6	53.4	−2.9	156.1	62.4	5.8	253	−0.721	116	−0.235
40	5.4	13.3	120.4	10.3	127.5	1.00	24	41	147.0	105.6	53.8	−2.9	156.5	62.7	5.9	254	−0.726	119	−0.240
41	5.2	12.8	120.4	31.0	124.1	0.95	25	45	180.0	105.6	53.4	−2.9	156.1	83.0	26.5	273	−0.864	184	−0.435
42	5.8	14.3	130.0	31.0	141.3	0.91	27	56	255.0	123.1	59.8	−3.4	179.5	89.0	26.1	276	−0.902	172	−0.408
43	5.5	13.5	134.0	10.3	153.4	0.99	26	48	189.0	130.7	63.4	−3.6	190.5	71.8	4.9	261	−0.782	107	−0.215

$D = 0.500$ mm, $t_w = 0.125$ mm, material: Cu–Ni 30%																			
44	4.8	9.6	20.0	31.0	4.5	1.03	24	55	94.0	2.9	2.1	−0.1	4.9	33.0	30.8	215	−0.527	168	−0.410
45	5.6	11.2	20.0	31.0	4.8	1.02	25	59	95.2	2.9	2.1	−0.1	4.9	33.0	30.8	214	−0.525	160	−0.390
46	5.0	10.0	40.0	31.0	15.2	1.05	24	48	144.2	11.7	6.6	−0.5	17.8	37.3	30.3	222	−0.557	176	−0.427
47	5.4	10.8	40.0	31.0	15.9	0.98	25	55	142.0	11.7	6.6	−0.5	17.8	37.3	30.3	221	−0.554	173	−0.420
48	5.0	10.0	60.0	31.0	31.0	0.94	25	52	193.0	26.2	12.9	−1.1	38.1	43.2	29.5	230	−0.595	177	−0.428
49	5.3	10.6	60.0	31.0	31.7	1.00	25	49	187.0	26.2	12.9	−1.1	38.1	43.2	29.5	230	−0.594	176	−0.426
50	4.9	9.8	100.0	31.0	96.6	1.00	27	51	264.0	72.6	29.8	−3.0	99.4	58.7	27.0	247	−0.692	176	−0.420
51	5.5	11.0	100.0	31.0	93.8	1.01	29	56	272.0	72.6	29.4	−3.0	99.0	58.2	27.2	244	−0.683	171	−0.407
$D = 0.635$ mm, $t_w = 0.203$ mm, material: Cu–Ni 30%																			
52	5.3	8.3	20.0	31.0	3.5	0.99	25	55	100.0	2.9	1.5	−0.2	4.3	32.4	30.8	213	−0.520	170	−0.415
53	5.0	7.9	20.0	31.0	3.0	1.02	25	53	97.0	2.9	1.5	−0.2	4.3	32.4	30.8	213	−0.520	174	−0.423
54	5.2	8.2	40.0	31.0	11.0	1.07	27	51	146.0	11.6	4.8	−0.8	15.7	35.2	30.1	216	−0.536	178	−0.432
55	5.2	8.2	40.0	31.0	14.1	1.00	25	50	150.0	11.6	4.9	−0.8	15.7	35.3	30.1	218	−0.541	180	−0.435
$D = 0.902$ mm, $t_w = 0.089$ mm, material: AISI SS-304																			
56	5.6	6.2	5.0	3.4	0.4	0.97	25	47	35.0	0.2	0.1	0.0	0.3	3.5	3.4	114	−0.223	72	−0.140
57	20.5	22.7	5.0	3.4	0.4	1.00	19	54	13.1	0.2	0.2	0.0	0.4	3.6	3.4	121	−0.238	62	−0.122
58	18.3	20.3	5.0	3.4	0.4	0.98	21	57	14.2	0.2	0.2	0.0	0.4	3.6	3.4	119	−0.234	62	−0.122
59	19.7	21.8	5.0	3.4	0.5	1.38	20	53	11.0	0.2	0.2	0.0	0.4	3.6	3.4	120	−0.236	72	−0.141
60	21.5	23.8	5.0	3.4	0.5	1.21	29	69	12.3	0.2	0.2	0.0	0.4	3.6	3.4	111	−0.218	53	−0.104
61	20.8	23.1	5.0	3.4	0.4	1.09	39	68	10.7	0.2	0.2	0.0	0.4	3.6	3.4	101	−0.198	52	−0.101
62	21.2	23.5	5.0	3.4	0.4	1.14	48	79	9.4	0.2	0.2	0.0	0.3	3.6	3.4	92	−0.180	48	−0.094
63	5.6	6.2	5.0	10.3	0.3	0.75	25	45	24.0	0.2	0.1	0.0	0.3	10.4	10.3	156	−0.331	128	−0.271
64	5.6	6.2	5.0	10.3	0.4	0.62	23	46	26.0	0.2	0.1	0.0	0.3	10.4	10.3	158	−0.335	127	−0.270
65	11.2	12.4	5.0	10.3	0.4	0.69	25	60	21.0	0.2	0.1	0.0	0.3	10.4	10.3	157	−0.332	107	−0.226
66	5.7	6.3	5.0	31.0	0.4	0.84	24	62	44.0	0.2	0.1	0.0	0.3	31.1	31.0	212	−0.513	159	−0.388
67	5.4	6.0	5.0	31.0	—	—	25	57	47.0	0.2	0.1	0.0	0.3	31.1	31.0	211	−0.511	157	−0.384
68	10.9	12.1	5.0	31.0	0.4	1.11	25	83	39.2	0.2	0.1	0.0	0.3	31.1	31.0	211	−0.511	120	−0.298
69	15.4	17.1	5.0	31.0	0.5	1.46	25	102	37.3	0.2	0.2	0.0	0.3	31.2	31.0	211	−0.511	90	−0.225
70	20.8	23.1	5.0	31.0	0.4	1.24	25	99	28.0	0.2	0.2	0.0	0.4	31.2	31.0	211	−0.512	88	−0.221
71	21.0	23.3	5.0	31.0	0.5	1.47	24	110	30.4	0.2	0.2	0.0	0.4	31.2	31.0	212	−0.514	78	−0.196
72	26.1	28.9	5.0	31.0	0.5	1.14	24	117	27.0	0.2	0.3	0.0	0.5	31.3	31.0	212	−0.515	64	−0.163
73	30.8	34.1	5.0	31.0	0.5	1.46	24	124	24.0	0.2	0.3	0.0	0.5	31.3	31.0	212	−0.515	57	−0.146
74	5.6	6.2	5.0	51.7	0.4	1.16	25	69	57.0	0.2	0.1	0.0	0.3	51.8	51.7	241	−0.651	174	−0.477
75	5.4	6.0	5.0	69.0	0.5	0.93	25	58	47.5	0.2	0.1	0.0	0.3	69.1	69.0	260	−0.767	206	−0.615
76	5.5	6.1	5.0	100.0	0.3	0.88	26	56	43.0	0.2	0.1	0.0	0.3	100.1	100.0	285	−0.992	236	−0.831

Table 1
Continued

Test no.	L (mm)	L/D	$G\times10^{-3}$ (kg m^{-2} s^{-1})	$P_{p,o}$ (bars)	$\Delta P = P_{p,i} - P_{p,o}$ (bars)	$\Delta P/\Delta P_{SP}$ (bars)	T_i (°C)	T_o (°C)	$q_m\times10^{-6}$ (W m^{-2})	ΔP_c (bars)	ΔP_f (bars)	ΔP_e (bars)	ΔP_{pred} (bars)	P_i (bars)	P_o (bars)	$\Delta T_{sub,i}$ (°C)	x_i	$\Delta T_{sub,o}$ (°C)	x_o
$D = 0.902$ mm, $t_w = 0.089$ mm, material: AISI SS-304																			
77	5.5	6.1	5.0	137.9	0.5	1.04	25	55	42.6	0.2	0.1	0.0	0.3	138.0	137.9	311	−1.351	261	−1.158
78	5.5	6.1	5.0	172.4	0.5	1.02	25	49	35.3	0.2	0.1	0.0	0.3	172.5	172.4	329	−1.905	288	−1.697
79	5.7	6.3	5.0	172.4	0.5	1.02	25	51	35.0	0.2	0.1	0.0	0.3	172.5	172.4	329	−1.905	287	−1.691
80	5.7	6.3	10.0	3.4	1.0	1.00	25	44	45.7	0.7	0.3	−0.1	0.9	3.6	3.3	115	−0.227	85	−0.165
81	5.1	5.7	10.0	10.3	1.3	0.80	24	42	43.6	0.7	0.3	−0.1	1.0	10.5	10.2	158	−0.335	133	−0.282
82	5.5	6.1	10.0	10.3	1.7	1.00	24	37	32.0	0.7	0.3	−0.1	1.0	10.5	10.2	158	−0.335	138	−0.292
83	10.7	11.9	10.0	10.3	1.5	1.00	25	-	29.0	0.7	0.4	−0.1	1.1	10.7	10.2	158	−0.335	123	−0.261
84	5.6	6.2	10.0	31.0	1.6	1.04	25	55	69.0	0.7	0.3	−0.1	0.9	31.2	30.9	211	−0.512	170	−0.414
85	5.5	6.1	10.0	31.0	1.7	1.00	25	58	73.0	0.7	0.3	−0.1	0.9	31.2	30.9	211	−0.512	168	−0.410
86	9.7	10.8	10.0	31.0	1.7	1.00	25	72	59.7	0.7	0.4	−0.1	1.1	31.4	30.9	211	−0.513	149	−0.366
87	5.6	6.2	15.0	3.4	3.1	0.91	24	42	59.8	1.6	0.6	−0.2	2.0	3.8	3.2	118	−0.233	88	−0.172
88	21.0	23.3	15.0	3.4	2.3	0.95	18	41	21.0	1.6	1.4	−0.2	4.6	4.6	3.2	131	−0.261	87	−0.169
89	20.8	23.1	15.0	3.4	2.6	1.00	19	56	25.0	1.6	1.4	−0.2	2.8	4.6	3.2	130	−0.259	80	−0.157
90	20.7	22.9	15.0	3.4	3.0	0.94	20	57	30.3	1.6	1.4	−0.2	2.8	4.6	3.2	129	−0.257	72	−0.140
91	20.5	22.7	15.0	3.4	2.7	1.09	30	59	26.0	1.6	1.3	−0.2	2.7	4.5	3.2	118	−0.235	68	−0.133
92	20.8	23.1	15.0	3.4	2.9	1.07	33	64	26.6	1.6	1.3	−0.2	2.7	4.5	3.2	115	−0.229	64	−0.125
93	20.2	22.4	15.0	3.4	2.7	1.20	39	70	25.3	1.6	1.2	−0.2	2.6	4.4	3.2	108	−0.216	61	−0.119
94	21.0	23.3	15.0	3.4	3.1	1.15	49	76	22.9	1.6	1.2	−0.2	2.6	4.4	3.2	98	−0.195	53	−0.103
95	20.4	22.6	15.0	3.4	2.8	1.17	60	84	19.7	1.6	1.1	−0.2	2.5	4.3	3.2	86	−0.172	47	−0.092
96	20.7	22.9	15.0	3.4	2.9	1.07	60	81	19.7	1.6	1.1	−0.2	2.5	4.3	3.2	86	−0.172	47	−0.092
97	20.5	22.7	15.0	3.4	3.0	1.07	70	89	16.5	1.6	1.1	−0.2	2.5	4.3	3.2	76	−0.151	42	−0.082
98	21.3	23.6	15.0	3.4	3.1	1.13	70	88	17.0	1.6	1.1	−0.2	2.5	4.3	3.2	76	−0.151	40	−0.079
99	20.5	22.7	15.0	3.4	3.7	1.56	70	98	20.3	1.6	1.1	−0.2	2.5	4.3	3.2	76	−0.151	36	−0.071
100	5.6	6.2	15.0	10.3	3.3	1.01	23	39	56.0	1.6	0.6	−0.2	2.0	10.7	10.1	160	−0.340	135	−0.286
101	5.8	6.4	15.0	10.3	3.4	0.94	25	40	51.0	1.6	0.6	−0.2	2.0	10.7	10.1	158	−0.335	135	−0.284
102	10.5	11.6	15.0	10.3	2.3	1.09	27	50	38.0	1.6	0.9	−0.2	2.3	11.0	10.1	157	−0.334	125	−0.265
103	16.0	17.7	15.0	10.3	2.9	0.91	25	41	36.0	1.6	1.1	−0.2	2.5	11.2	10.1	160	−0.341	115	−0.243
104	20.2	22.4	15.0	10.3	2.2	0.92	24	55	26.0	1.6	1.4	−0.2	2.8	11.5	10.1	162	−0.346	119	−0.253
105	21.6	23.9	15.0	10.3	2.3	0.81	25	64	30.4	1.6	1.3	−0.2	2.8	11.4	10.1	161	−0.343	109	−0.231
106	25.7	28.5	15.0	10.3	2.5	0.98	24	66	28.0	1.6	1.6	−0.2	3.0	11.7	10.1	163	−0.348	106	−0.224
107	26.2	29.0	15.0	10.3	3.4	0.96	24	53	22.0	1.6	1.8	−0.2	3.2	12.0	10.1	164	−0.351	116	−0.245
108	15.8	17.5	15.0	31.0	2.6	1.02	25	78	57.0	1.6	1.1	−0.2	2.5	31.9	30.8	212	−0.517	147	−0.360
109	20.1	22.3	15.0	31.0	3.2	1.08	25	92	57.5	1.6	1.3	−0.2	2.8	32.2	30.8	212	−0.519	129	−0.318
110	5.3	5.9	15.0	31.0	3.8	1.04	24	47	74.0	1.6	0.6	−0.2	2.0	31.4	30.8	212	−0.516	184	−0.446
111	5.5	6.1	15.0	31.0	3.0	1.00	25	51	85.0	1.6	0.6	−0.2	2.0	31.4	30.8	211	−0.513	177	−0.431
112	10.6	11.8	15.0	31.0	2.6	0.82	25	62	59.6	1.6	0.9	−0.2	2.3	31.7	30.8	212	−0.515	166	−0.404
113	25.2	27.9	15.0	31.0	2.8	1.17	25	85	46.0	1.6	1.6	−0.2	3.0	32.4	30.8	213	−0.520	129	−0.317
114	27.0	29.9	15.0	31.0	3.1	1.14	25	107	52.0	1.6	1.8	−0.2	3.2	32.6	30.8	213	−0.522	111	−0.277
115	5.7	6.3	15.0	51.7	3.0	1.02	25	52	84.0	1.6	0.6	−0.2	2.0	52.1	51.5	241	−0.654	207	−0.563
116	5.0	5.5	15.0	69.0	3.8	1.02	25	48	83.0	1.6	0.6	−0.2	2.0	69.4	68.8	260	−0.769	231	−0.683
117	6.0	6.7	15.0	100.0	3.9	0.97	24	49	76.0	1.6	0.6	−0.2	2.0	100.4	99.8	288	−1.001	255	−0.893
118	5.7	6.3	15.0	137.9	4.7	0.96	25	48	72.0	1.6	0.6	−0.2	2.0	138.3	137.7	311	−1.356	282	−1.236
119	5.7	6.3	15.0	137.9	2.6	0.99	25	48	72.0	1.6	0.6	−0.2	2.0	138.3	137.7	311	−1.356	282	−1.236
120	5.3	5.9	15.0	172.4	2.8	0.99	27	44	59.0	1.6	0.6	−0.2	2.0	172.8	172.2	327	−1.902	305	−1.778

$D = 0.902$ mm, $t_w = 0.089$ mm, material: AISI SS-304

121	11.0	12.2	16.1	27.9	3.1	1.00	24	58	51.3	1.9	1.0	−0.2	2.6	28.7	27.6	207	−0.496	168	−0.402
122	13.6	15.1	16.1	26.6	4.5	0.93	23	59	47.5	1.9	1.3	−0.2	2.9	27.6	26.3	206	−0.490	161	−0.383
123	20.5	22.7	16.1	27.6	3.5	1.11	23	69	38.0	1.9	1.5	−0.2	3.2	28.9	27.3	209	−0.500	155	−0.370
124	5.7	6.3	20.0	3.4	-	-	23	37	63.0	2.9	1.0	−0.4	3.5	4.1	3.0	122	−0.241	92	−0.179
125	5.9	6.5	20.0	3.4	3.8	0.92	25	38	55.0	2.9	1.0	−0.4	3.5	4.1	3.0	119	−0.236	92	−0.179
126	5.8	6.4	20.0	10.3	4.5	0.87	24	44	75.0	2.9	1.0	−0.4	3.5	11.0	9.9	160	−0.340	133	−0.280
127	6.1	6.8	20.0	10.3	3.0	0.98	25	43	68.0	2.9	1.0	−0.4	3.5	11.0	9.9	159	−0.338	133	−0.280
128	10.4	11.5	20.0	10.3	5.9	0.89	25	53	50.0	2.9	1.4	−0.4	3.9	11.4	9.9	160	−0.342	127	−0.268
129	5.5	6.1	20.0	31.0	3.7	1.06	25	45	79.0	2.9	1.0	−0.4	3.5	31.7	30.6	212	−0.515	187	−0.454
130	5.7	6.3	20.0	31.0	5.5	0.96	25	47	90.6	2.9	1.0	−0.4	3.5	31.7	30.6	212	−0.515	183	−0.444
131	5.8	6.4	20.0	31.0	4.9	0.97	25	48	92.0	2.9	1.0	−0.4	3.5	31.7	30.6	212	−0.515	182	−0.441
132	11.0	12.2	20.0	31.0	3.9	1.12	26	63	72.5	2.9	1.4	−0.4	3.9	32.0	30.6	211	−0.515	167	−0.406
133	5.8	6.4	30.0	3.4	7.6	1.00	24	33	56.0	6.4	2.0	−0.8	7.6	4.6	2.5	125	−0.250	92	−0.179
134	21.0	23.3	30.0	3.4	8.6	1.04	20	52	49.1	6.4	4.4	−0.8	10.0	7.1	2.5	145	−0.298	72	−0.139
135	20.1	22.3	30.0	3.4	9.7	1.08	20	55	54.7	6.4	4.4	−0.8	10.0	7.1	2.5	145	−0.298	69	−0.134
136	20.7	22.9	30.0	3.4	9.7	1.08	21	56	54.0	6.4	4.4	−0.8	10.0	7.0	2.5	144	−0.296	68	−0.131
137	20.9	23.2	30.0	3.4	11.4	1.10	37	72	53.0	6.4	3.9	−0.8	9.5	6.6	2.5	125	−0.256	52	−0.101
138	20.8	23.1	30.0	3.4	12.4	0.84	41	78	55.0	6.4	3.8	−0.8	9.5	6.5	2.5	121	−0.246	47	−0.090
139	20.9	23.2	30.0	3.4	10.3	1.25	47	82	47.0	6.4	3.7	−0.8	9.3	6.3	2.5	114	−0.232	46	−0.090
140	20.0	22.2	30.0	3.4	11.0	1.48	56	91	46.0	6.5	3.6	−0.8	9.2	6.2	2.5	104	−0.211	39	−0.076
141	18.8	20.8	30.0	3.4	11.0	1.50	67	97	43.0	6.5	3.4	−0.8	9.0	6.0	2.5	92	−0.187	32	−0.062
142	5.9	6.5	30.0	10.3	11.4	0.94	25	44	98.0	6.4	2.0	−0.8	7.6	11.5	9.4	161	−0.344	132	−0.278
143	4.6	5.1	30.0	31.0	8.3	1.09	25	40	108.0	6.4	2.0	−0.8	7.6	32.2	30.1	213	−0.519	191	−0.463
144	12.0	13.3	31.9	31.0	9.0	0.93	26	50	64.5	7.3	3.0	−0.9	9.4	33.1	30.0	213	−0.523	182	−0.441
145	11.5	12.7	37.2	31.0	13.8	0.98	26	52	81.4	9.9	3.9	−1.3	12.5	33.7	29.7	214	−0.527	181	−0.436
146	5.7	6.3	40.0	10.3	20.3	0.92	25	42	123.0	11.4	3.2	−1.5	13.1	12.1	8.7	163	−0.351	131	−0.273
147	5.7	6.3	40.0	10.3	13.5	0.98	24	40	117.0	11.4	3.2	−1.5	13.2	12.2	8.7	165	−0.353	133	−0.277
148	5.7	6.3	40.0	31.0	13.1	0.95	25	43	127.0	11.4	3.2	−1.5	13.1	32.8	29.4	214	−0.523	189	−0.454
149	5.4	6.0	40.0	31.0	12.4	0.90	25	40	118.0	11.4	3.2	−1.5	13.1	32.9	29.4	214	−0.524	191	−0.460
150	5.9	6.5	40.0	51.7	12.1	0.95	24	40	119.0	11.4	3.2	−1.5	13.2	53.6	50.2	244	−0.666	221	−0.596
151	5.0	5.5	40.0	51.7	13.1	0.95	24	38	119.0	11.4	3.2	−1.5	13.2	53.6	50.1	244	−0.666	224	−0.603
152	5.5	6.1	40.0	69.0	18.6	0.90	25	43	132.0	11.4	3.2	−1.5	13.1	70.8	67.4	262	−0.779	239	−0.703
153	5.8	6.4	40.0	100.0	14.5	1.05	26	47	149.0	11.4	3.2	−1.5	13.1	101.8	98.4	287	−1.006	262	−0.906
154	5.2	5.8	40.0	137.9	17.2	1.00	27	48	159.0	11.4	3.2	−1.5	13.1	139.7	136.3	310	−1.364	286	−1.240
155	5.3	5.9	40.0	137.9	17.9	0.95	26	41	113.6	11.4	3.2	−1.5	13.1	139.7	136.3	311	−1.368	293	−1.267
156	5.9	6.5	40.0	172.4	17.2	1.11	28	48	136.0	11.4	3.2	−1.5	13.1	174.2	170.9	326	−1.928	304	−1.749
157	5.1	5.7	60.0	31.0	30.3	1.01	26	39	153.0	25.5	6.3	−3.3	28.5	34.2	27.5	215	−0.531	189	−0.451
158	5.1	5.7	60.0	31.0	31.4	0.95	26	39	155.0	25.5	6.3	−3.3	28.5	34.2	27.5	215	−0.531	189	−0.450
159	5.8	6.4	60.0	31.0	30.3	0.94	25	42	171.0	25.5	6.3	−3.3	28.6	34.2	27.5	216	−0.533	187	−0.445
160	5.9	6.5	60.0	31.0	31.0	0.96	25	38	135.0	25.5	6.3	−3.3	28.6	34.2	27.5	216	−0.533	190	−0.453
161	5.2	5.8	63.7	82.8	29.3	0.89	24	38	138.0	28.8	7.0	−3.7	32.1	86.4	78.9	277	−0.891	258	−0.803
162	6.1	6.8	95.5	82.8	63.8	0.93	29	42	193.0	64.5	13.4	−8.4	69.5	88.1	74.1	273	−0.889	248	−0.753
163	4.5	5.0	100.0	31.0	67.6	0.97	26	34	173.5	70.6	14.7	−9.2	76.2	37.1	21.3	220	−0.551	181	−0.416
164	6.1	6.8	100.7	97.9	71.0	1.00	31	45	206.0	71.7	14.4	−9.3	76.8	103.4	88.2	283	−1.002	258	−0.844

Table 1
Continued

Test no.	L (mm)	L/D	$G\times10^{-3}$ (kg m^{-2} s^{-1})	$P_{p,o}$ (bars)	$\Delta P = P_{p,i}-P_{p,o}$ (bars)	$\Delta P/\Delta P_{SP}$ (bars)	T_i (°C)	T_o (°C)	$q_m\times10^{-6}$ (W m^{-2})	ΔP_c (bars)	ΔP_f (bars)	ΔP_e (bars)	ΔP_{pred} (bars)	P_i (bars)	P_o (bars)	$\Delta T_{sub,i}$ (°C)	x_i	$\Delta T_{sub,o}$ (°C)	x_o
$D = 1.07$ mm, $t_w = 0.090$ mm, material: AISI SS-304																			
165	5.0	4.7	20.0	31.0	4.1	1.01	25	43	85.0	2.8	0.8	−0.5	3.2	31.4	30.5	211	−0.513	191	−0.462
166	5.1	4.8	20.0	31.0	3.5	1.00	25	43	87.0	2.8	0.8	−0.5	3.2	31.4	30.5	211	−0.513	190	−0.460
167	6.2	5.8	20.0	31.0	3.8	0.99	23	37	75.0	2.8	0.8	−0.5	3.2	31.4	30.5	213	−0.518	191	−0.463
168	5.5	5.1	40.0	31.0	9.0	0.93	24	37	116.0	11.2	2.7	−2.0	11.9	31.8	29.0	213	−0.518	194	−0.465
169	6.1	5.7	40.0	31.0	14.5	0.95	29	44	122.0	11.2	2.6	−2.0	11.8	31.7	29.0	208	−0.506	186	−0.448
170	5.2	4.9	60.0	31.0	26.6	1.01	25	37	156.0	25.1	5.2	−4.4	25.9	31.9	26.4	212	−0.517	190	−0.449
171	5.2	4.9	60.0	31.0	24.1	0.92	25	37	163.0	25.1	5.2	−4.4	25.9	31.9	26.4	212	−0.517	189	−0.448
172	6.0	5.6	60.0	31.0	24.1	0.97	25	38	147.0	25.1	5.2	−4.4	25.9	31.9	26.4	212	−0.517	189	−0.447
$D = 2.54$ mm, $t_w = 0.105$ mm, material: AISI SS-304																			
173	6.0	2.4	20.0	31.0	0.2	0.96	22	41	60.0	0.7	0.3	−0.7	0.3	30.6	30.3	213	−0.515	205	−0.496
174	6.3	2.5	20.0	31.0	0.2	1.00	23	36	40.0	0.7	0.3	−0.7	0.3	30.6	30.3	212	−0.512	206	−0.499

Note: Diameter of inlet and outlet plenums was 2.83 mm; unheated regions (tube solder joints) immediately upstream and downstream of the heated section were assumed equal in length, $L_{uh} = 0.5(L_t - L)$; total length of tube, L_t, and heated length, L, were related by

$$L_t = \begin{cases} 11, & L \leqslant 9 \\ 16, & 9 < L \leqslant 13 \\ 21, & 13 < L \leqslant 18 \\ 26, & 18 < L \leqslant 23 \\ 31, & 23 < L \leqslant 26 \\ 36, & L > 26 \end{cases}$$

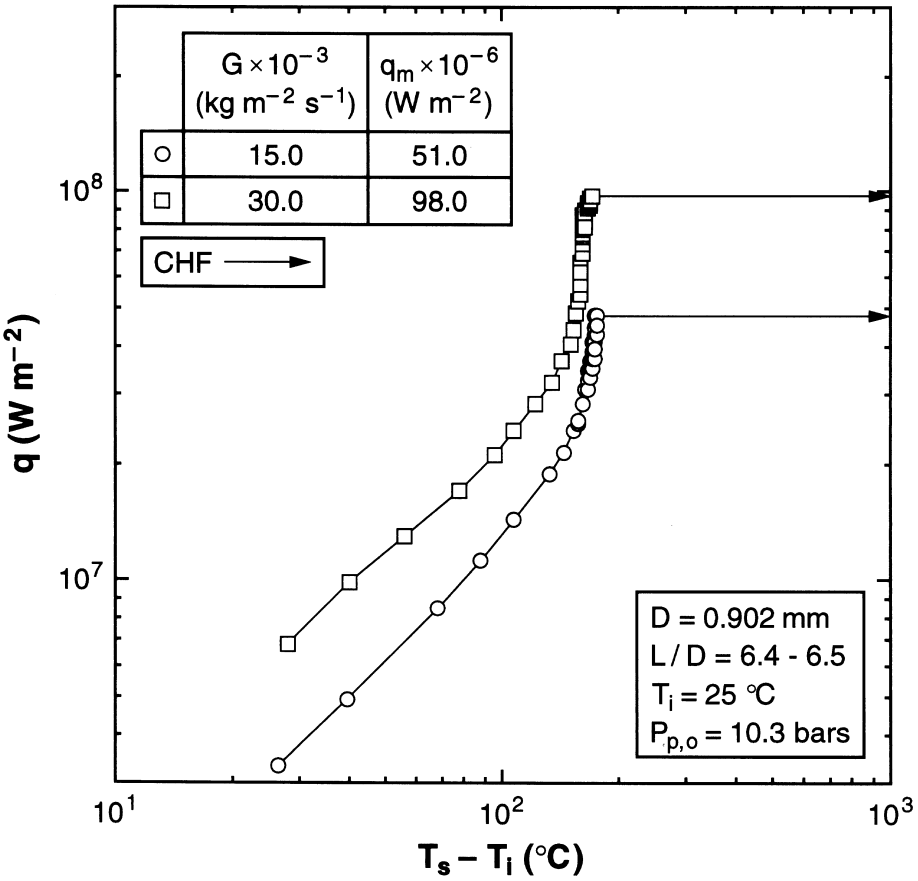

Fig. 6. Effect of mass velocity on boiling curve.

Although the tubes used in the present study were thin-walled (in order to increase electrical resistance for the purpose of matching the voltage–current characteristics of the power supply), wall thickness had no measurable effect on CHF. Interestingly, CHF is known to decrease slightly with decreasing wall thickness in typical low mass velocity flow boiling situations. This difference in wall thickness effect can be explained as follows. CHF is associated with build-up of intermittent vapor blankets whose size is determined by the Helmholtz wavelength and wall thickness can influence axial conduction within the wall during the passage of a vapor mass. A thinner tube offers greater resistance to the heat flow and, thus, may reduce CHF slightly in typical flow boiling situations. However, the Helmholtz wavelength in high mass velocity flows is very small and the wave speed very large. Therefore, the passage of a vapor mass at these extreme conditions will not produce any substantial transient temperature excursions in the wall. In other words, CHF is not influenced by wall thickness except for vanishingly small thicknesses.

4. Pressure drop characteristics

Pressure drop results for ultra-high heat flux conditions are presented in Fig. 9(a). Shown is the pressure drop vs heat flux at mass velocities of 40 000 and 100 000 kg m^{-2} s^{-1} for three different tube diameters. Also indicated is the length to diameter ratio for each based on both the heated length, L, and total length, L_t, which includes the unheated inlet and outlet regions of the tube. Referring to the three cases corresponding to the lower mass velocity, the pressure drop increased with decreasing tube diameter with the smallest diameter of 0.406 mm yielding a total pressure drop of approximately 20 bars. An increase in mass velocity to 100 000 kg m^{-2} s^{-1} resulted in large increases in pressure drop for all three diameters with the smaller diameter yielding a very high pressure drop in excess of 100 bars. Ultra-high heat fluxes about 200 MW m^{-2} were achieved only with very high mass velocities similar to those represented in Fig. 9(a) at the expense of very large pressure drops. However, in each case, there was little variation in pressure drop over the

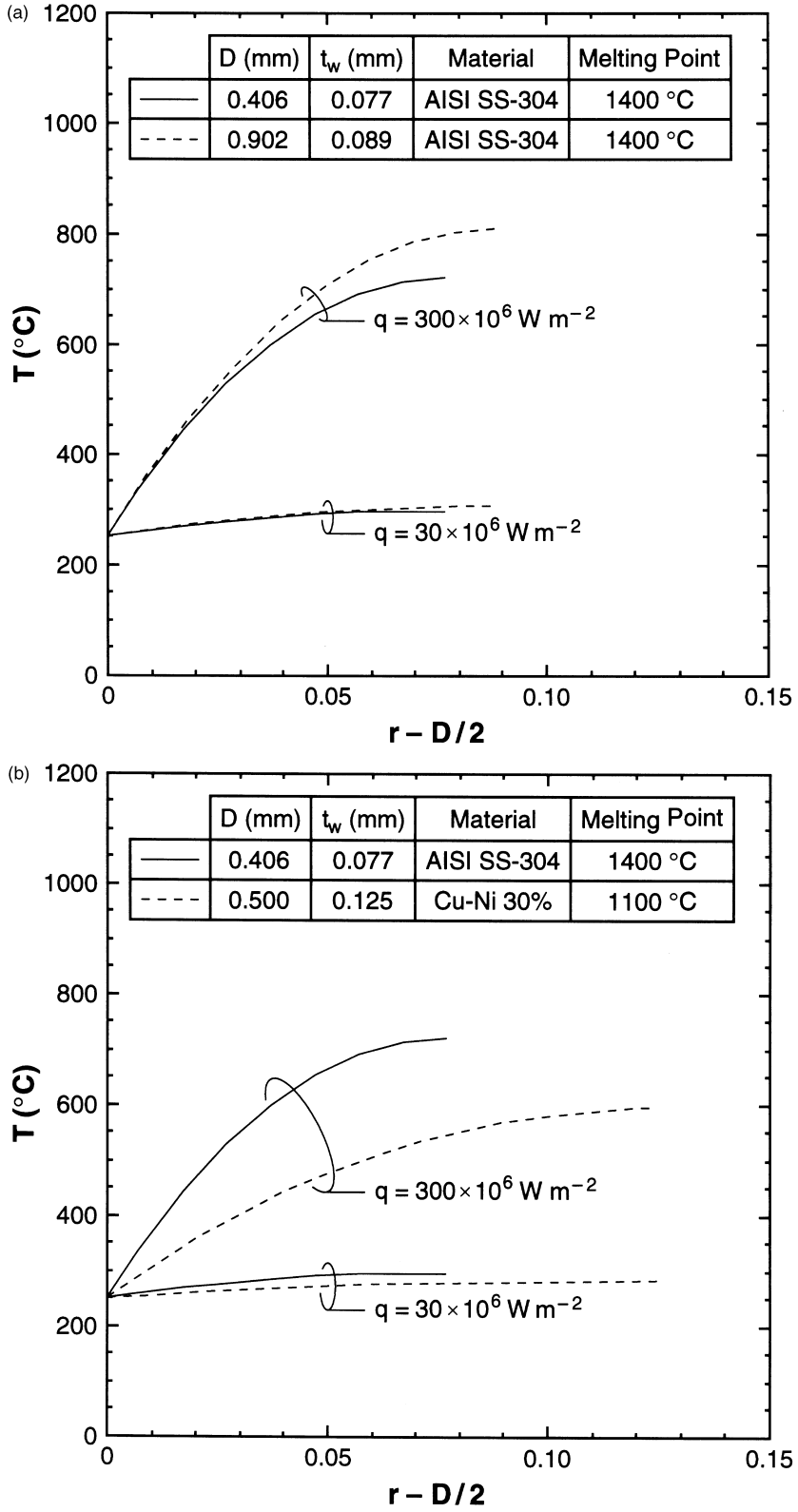

Fig. 7. Effect of (a) diameter and (b) material on temperature distribution through tube wall at relatively low and high heat fluxes assuming a temperature of 250°C at inner surface and an adiabatic outer surface.

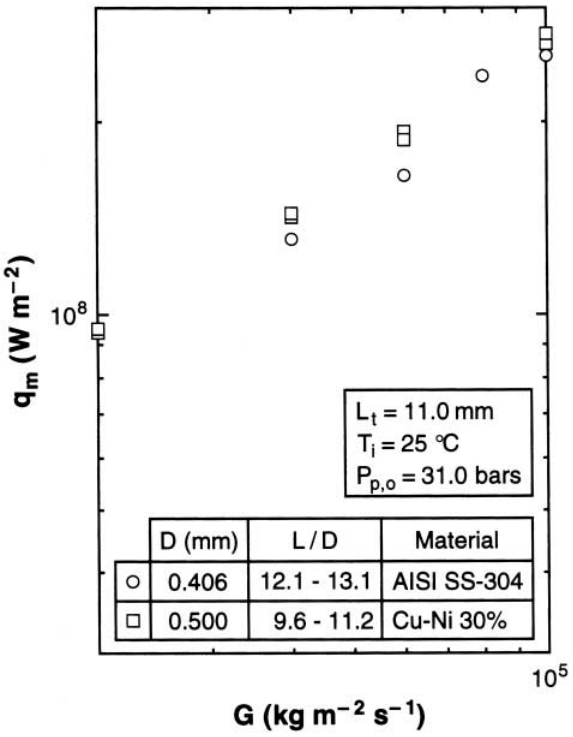

Fig. 8. Effect of tube material on CHF.

entire range of heat flux up to CHF. Beginning at low heat fluxes, where the flow was that of pure liquid, an increase in heat flux caused a slight decrease in pressure drop due to a reduction in liquid viscosity with increasing temperature. This trend was generally sustained until the heat flux neared CHF where a slight rise in the pressure drop was detected.

These cases are representative of the bulk of the data obtained in this study and clearly show that high pressure drop should be of great concern when designing a cooling system for ultra-high heat flux dissipation. Under these conditions, the coolant enters the test section subcooled and, as a result of the large mass velocity required to achieve ultra-high CHF, the flow remains subcooled at the exit, resulting in a predominantly single-phase pressure drop. The slight increase in pressure drop at heat fluxes near CHF is evidence of a small amount of vapor causing a minor increase in the frictional pressure drop; the accelerational pressure drop associated with net vapor generation is very small due to the high exit subcooling. Thus, a simple single-phase model seems most suitable for predicting the pressure drop for these conditions.

Figure 9(b) shows pressure drop data for 0.902 mm diameter tubes at relatively low mass velocities. For a more informative illustration, pressure drop in Fig. 9(b) is non-dimensionalized with respect to the single-phase adiabatic pressure drop (i.e., without heat generation in the tube wall). Two of the cases represented are for heated lengths greater than 20 mm and illustrate the effect of a long heated length on the total pressure drop. The case of the short heated length ($L = 5.8$ mm) corresponds to a boiling curve presented in Fig. 6. The short heated length exhibited behavior similar to the previously discussed trends for pressure drop; there was a slight reduction in pressure drop at low heat fluxes after which the pressure drop remained relatively constant. Overall, the total pressure drop for this case deviated from the single-phase pressure drop by less than 5%. Figure 9(b) also shows pressure drop for a longer tube ($L = 20.1$ mm) at the same mass velocity. A somewhat similar CHF value was achieved in the longer tube by increasing outlet plenum pressure to $P_{p,o} = 31.0$ bars. For this case, there is an initial reduction in pressure drop at low heat fluxes followed by a gradual rise in pressure drop with increasing heat flux; however, even for this relatively long tube, the pressure drop increased beyond the single-phase pressure drop by less than 10%. In contrast to the two examples just discussed, the third case for a relatively low mass velocity of 5000 kg m^{-2} s^{-1} in a tube approximately equal in length to the longer of the first two exhibited the appreciable rise (about 40%) in pressure drop with increasing heat flux common to most two-phase flow systems.

Overall, these examples show that pressure drop deviations from the single-phase pressure drop are significant only for small mass velocities ($G \leqslant 5000$ kg m^{-2} s^{-1}) and long tubes ($L/D \geqslant 20$). Equally important is the conclusion that pressure variations along the heated tube should be carefully assessed when acquiring or presenting ultra-high CHF data. This important issue will be explored in Part II of the present study [14].

5. Parametric CHF trends

As indicated above, the present ultra-high CHF data were acquired over broad ranges of both flow and geometrical parameters. A key tactic in the study was to explore the individual effects of key parameters while keeping all other parameters unchanged. The key parameters include tube diameter, heated length-to-diameter ratio, mass velocity, subcooling, and pressure. In this section, the trends resulting from these parametric tests will be discussed.

5.1. Effect of tube diameter

The effect of tube diameter for constant values of heated length, inlet temperature, and outlet plenum pressure is illustrated in Fig. 10. CHF data are shown for three mass velocities ranging from 20 000 to 60 000 kg m^{-2} s^{-1}. The plot shows a consistent trend of increasing

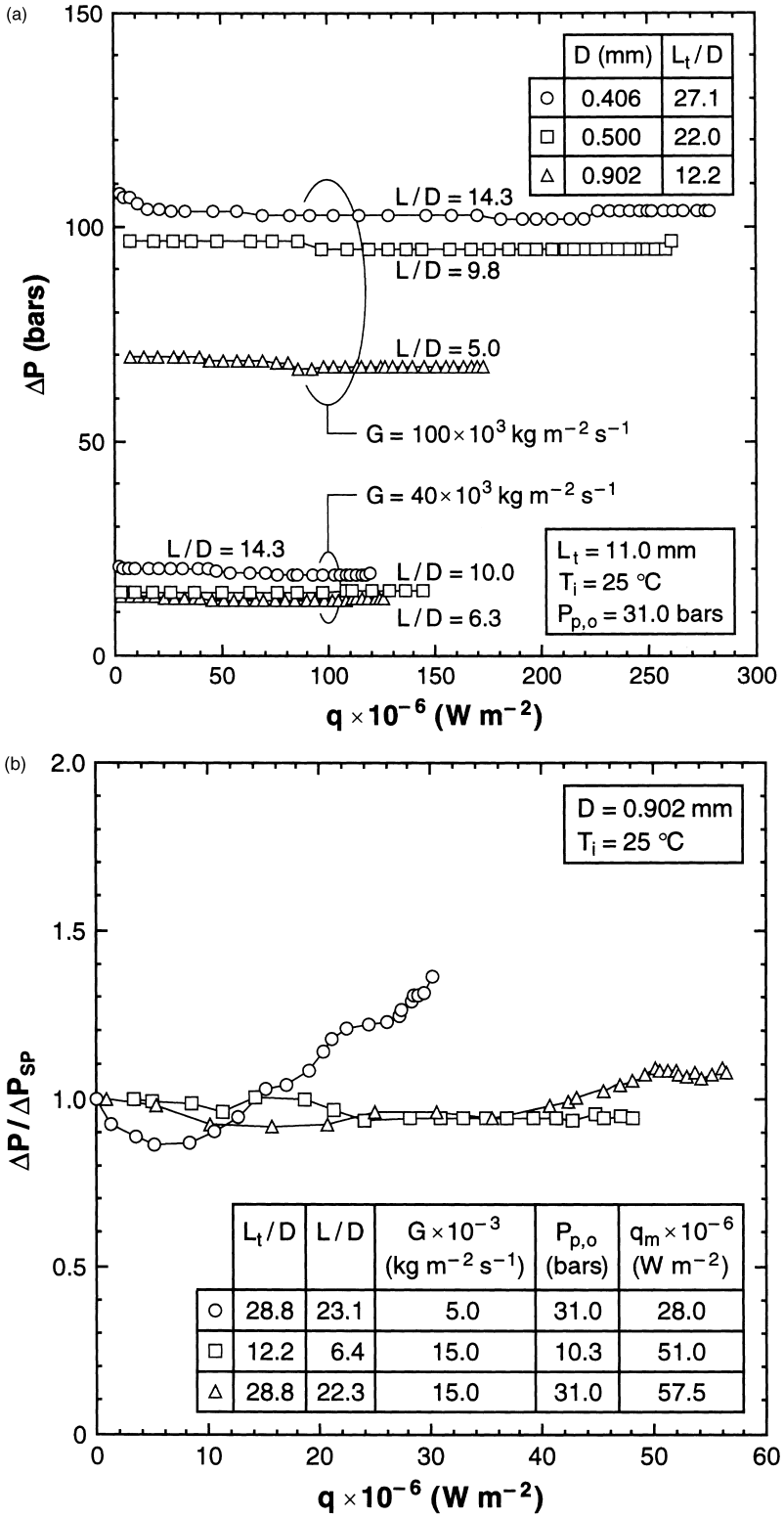

Fig. 9. Effect of heat flux on (a) pressure drop at high mass velocities and (b) ratio of pressure drop to adiabatic, single-phase pressure drop at relatively low mass velocities.

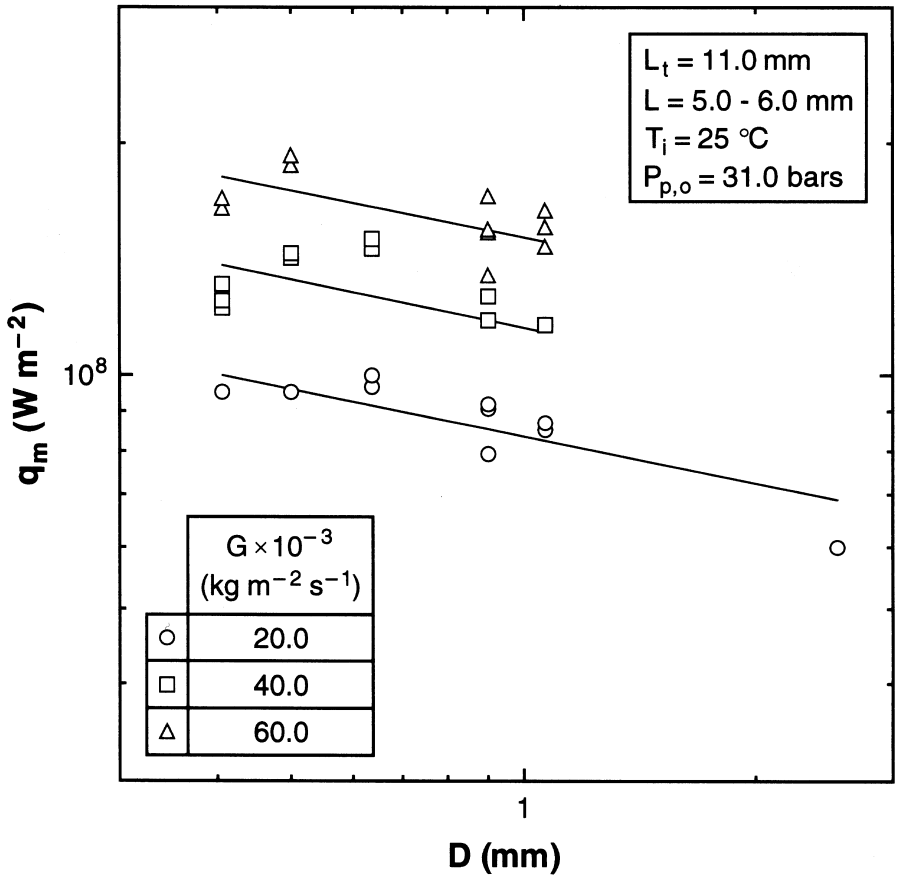

Fig. 10. Effect of diameter on CHF.

CHF with decreasing tube diameter. The data are well represented by curve fits of CHF proportional to $D^{-0.200}$.

5.2. Effect of heated length-to-diameter ratio

Figure 11(a) shows the effect of heated length-to-diameter ratio on CHF for mass velocities of 5000 and 15 000 kg m^{-2} s^{-1} and a constant outlet plenum pressure of 31.0 bars, where the heated length was varied from 5.5 to 31.0 mm. For both mass velocities, CHF decreased with increasing L/D ratio. Figure 11(b) shows similar trends for outlet plenum pressures of 10.3 and 31.0 bars at a mass velocity of 15 000 kg m^{-2} s^{-1}. Data in all these cases seem well represented by curve fits of CHF proportional to $(L/D)^{-0.324}$.

5.3. Effect of mass velocity

The effect of mass velocity on CHF at $P_{p,o} = 31.0$ bars is presented in Fig. 12(a) for tubes of $D = 0.406$ and 0.902 mm with equal lengths. A broad range of mass velocity is shown, from a moderate value of 5000 to a large value of 130 000 kg m^{-2} s^{-1}, which surpasses the mass velocities of any previous CHF study. Figure 12(a) shows CHF is proportional to $G^{0.446}$, with the smaller tube diameter yielding a higher CHF, despite its greater L/D ratio. Figure 12(b) shows the effect of mass velocity for $D = 0.902$ mm at exit plenum pressures of 3.4 and 31.0 bars. Both pressures produced the same characteristic increase in CHF with increasing mass velocity with the higher pressure yielding higher CHF values.

5.4. Effect of subcooling

The effect of inlet subcooling is illustrated in Fig. 13(a) for mass velocities of 5000, 15 000, and 30 000 kg m^{-2} s^{-1}. The cases illustrated are for a low pressure of $P_{p,o} = 3.4$ bars and a relatively long heated tube with $L/D = 20.3$ to 23.8; conditions chosen to yield the greatest subcooling effect. Inlet subcooling was calculated as the difference between the measured inlet temperature and the saturation temperature based on pressure at the beginning of the heated section. Figure 13(a) shows a fairly linear increase in CHF with increasing subcooling, with all three

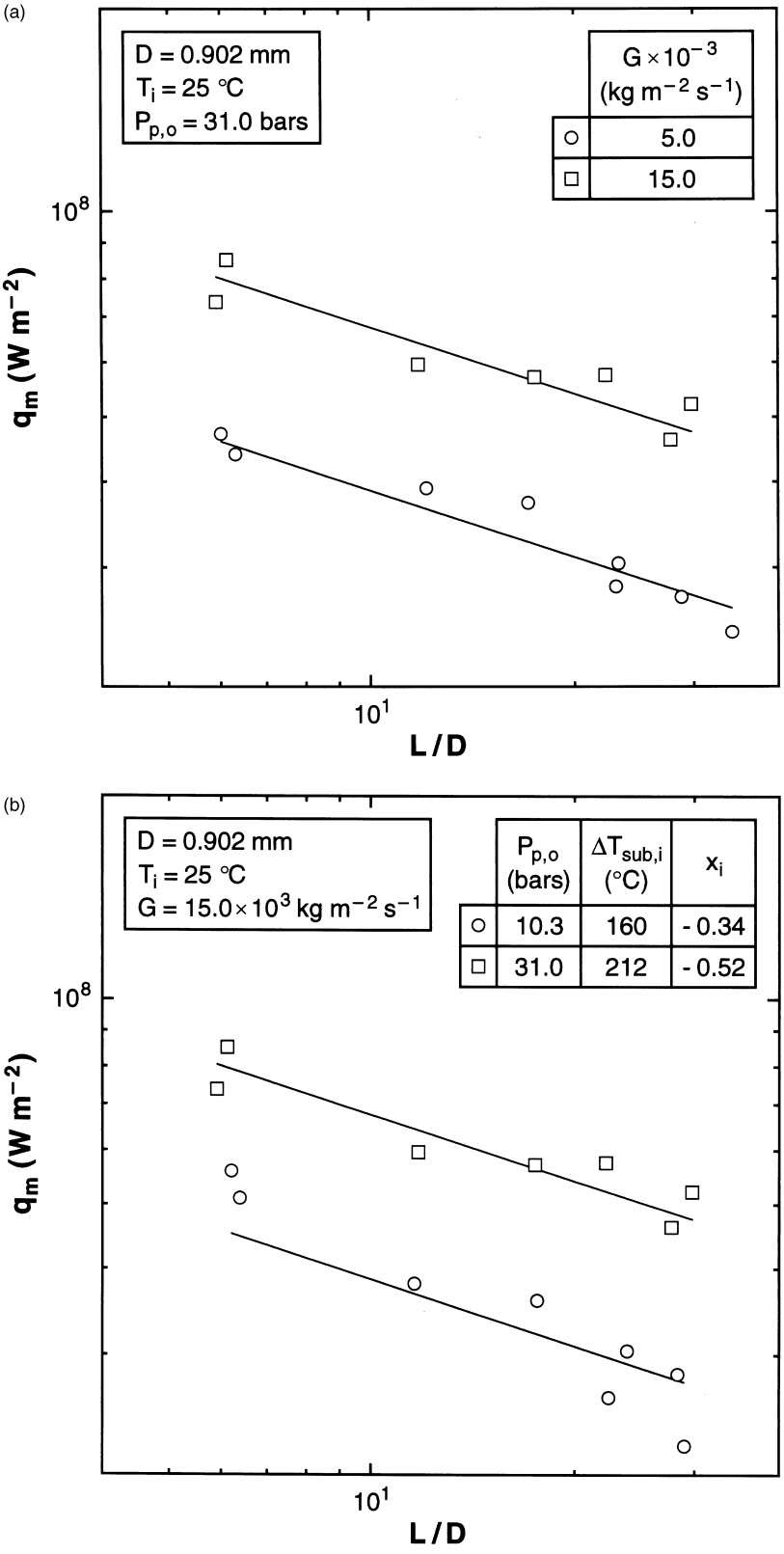

Fig. 11. Effect of heated length-to-diameter ratio on CHF for different (a) mass velocities and (b) outlet plenum pressures.

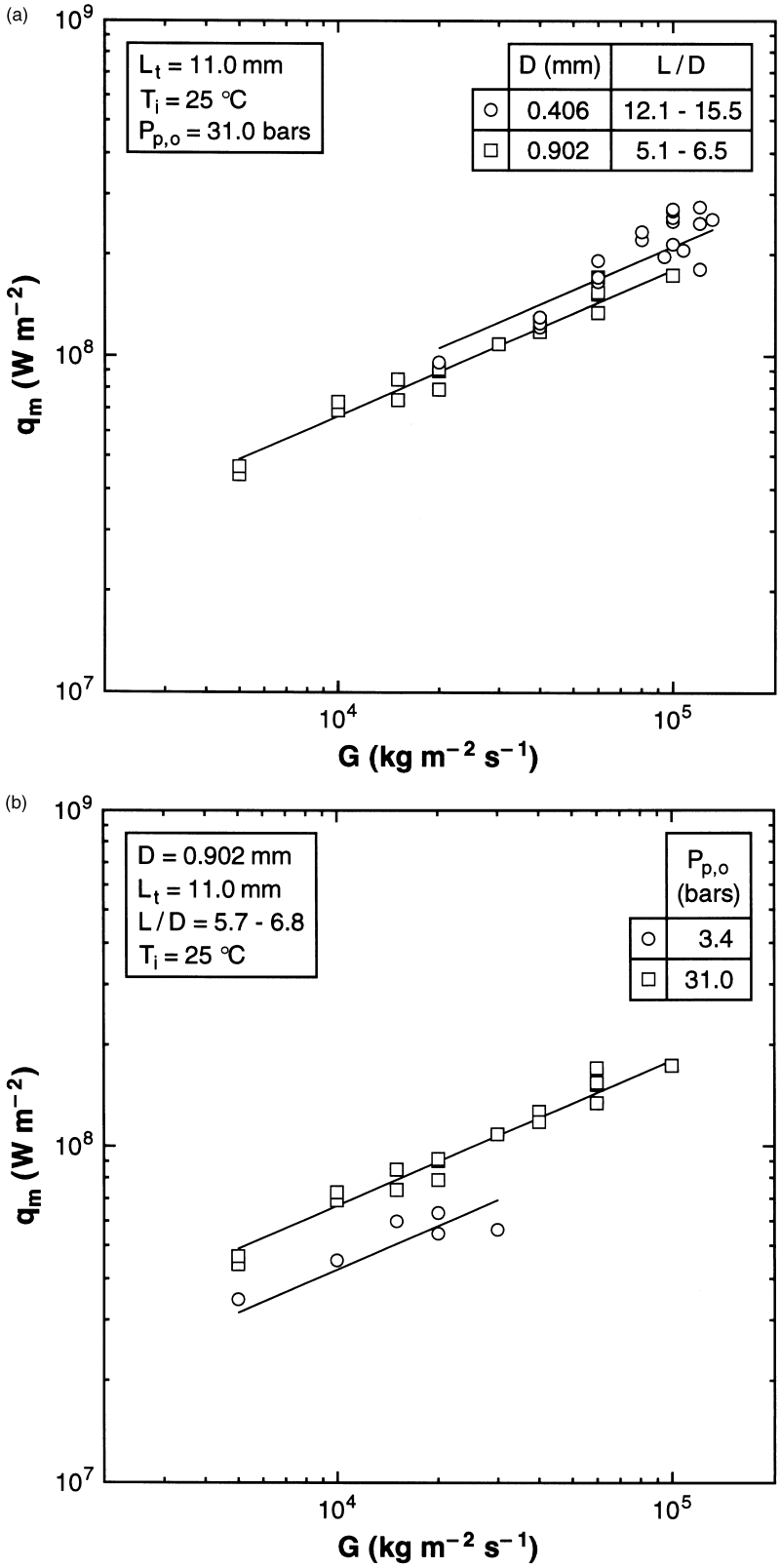

Fig. 12. Effect of mass velocity on CHF for different (a) diameters and (b) outlet pressures.

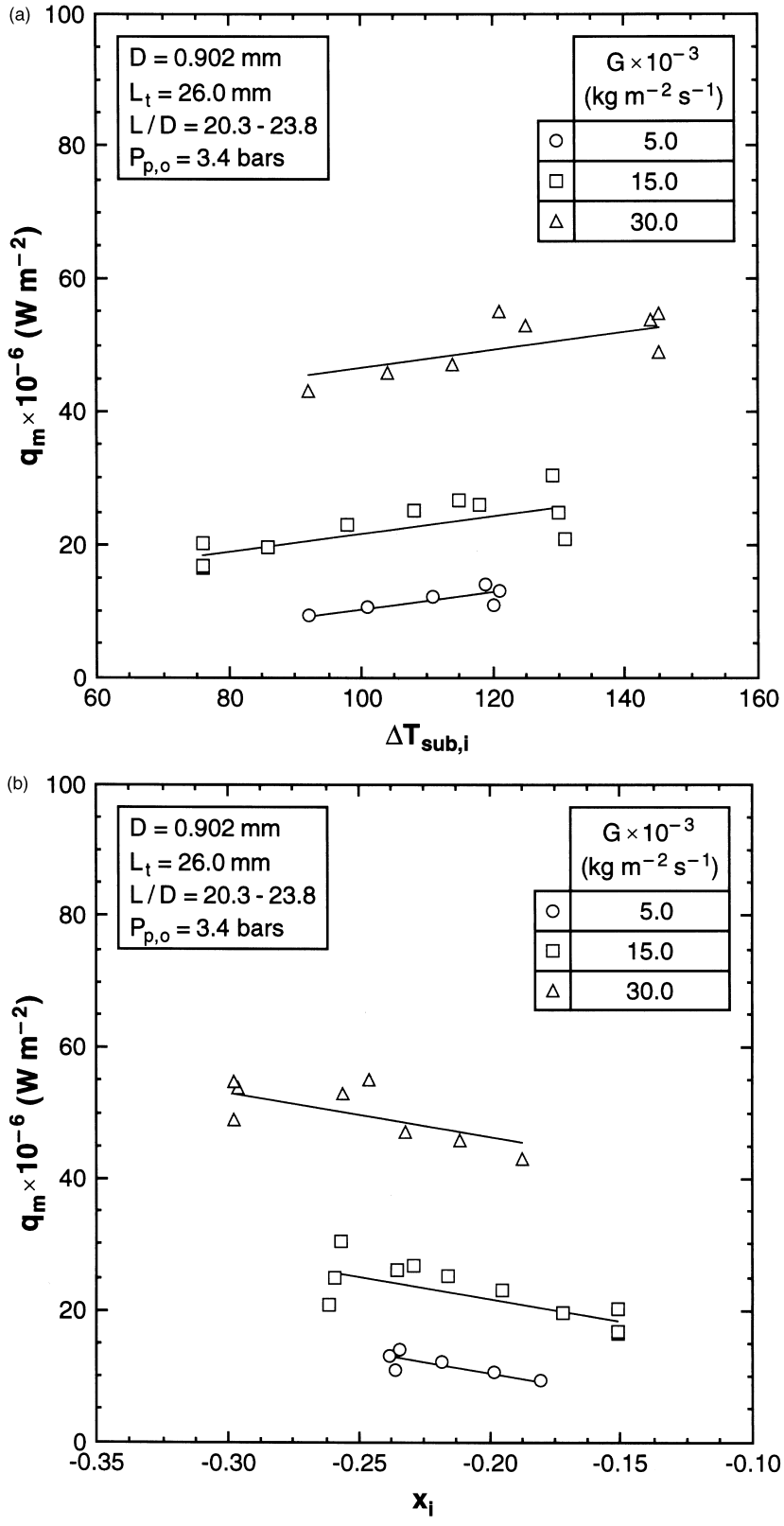

Fig. 13. Effect of (a) inlet subcooling and (b) inlet quality on CHF.

mass velocities exhibiting a similar slope and higher mass velocities producing higher CHF values. Figure 13(b) illustrates essentially the same trend revealed in Fig. 13(a) using inlet quality, x_i, instead of inlet subcooling.

5.5. Effect of pressure

Figure 14 shows the variation of CHF with pressure at the exit of the heated length. CHF data are presented for a single nominal heated length and three mass velocities over a broad pressure range of 3.2 to 172.4 bars. Unfortunately, the effect of pressure could not be isolated from that of subcooling since the pressure trend tests were performed by fixing inlet temperature rather than inlet subcooling. Subcooling for data corresponding to each mass velocity in Fig. 14 increases with increasing pressure for a constant inlet temperature; however, the increase in subcooling is smaller for high pressures, especially near the critical point. In any case, Fig. 14 shows a general trend of increasing CHF with increasing pressure up to about 30 bars, followed by a region from 30 to 150 bars where CHF showed little change with pressure. Critical heat flux then began decreasing as pressure was increased closer to the critical point. This overall trend is similar to that observed even in pool boiling and can be partially explained by property changes, especially those in latent heat of vaporization. Figure 14 further shows a reduced pressure effect for the highest mass velocity over the entire pressure range.

6. Conclusions

In order to develop design tools for applications requiring dissipation of ultra-high heat fluxes, an experimental investigation was conducted for subcooled flow boiling of water in small diameter tubes at high mass velocities. Ultra-high CHF data were obtained to ascertain the effects of tube diameter, heated length-to-diameter ratio, mass velocity, subcooling, and pressure on CHF. Key findings from the study are as follows:

1. Ultra-high CHF is accompanied by physical 'burnout' of the tube wall near the exit. Data for tubes made

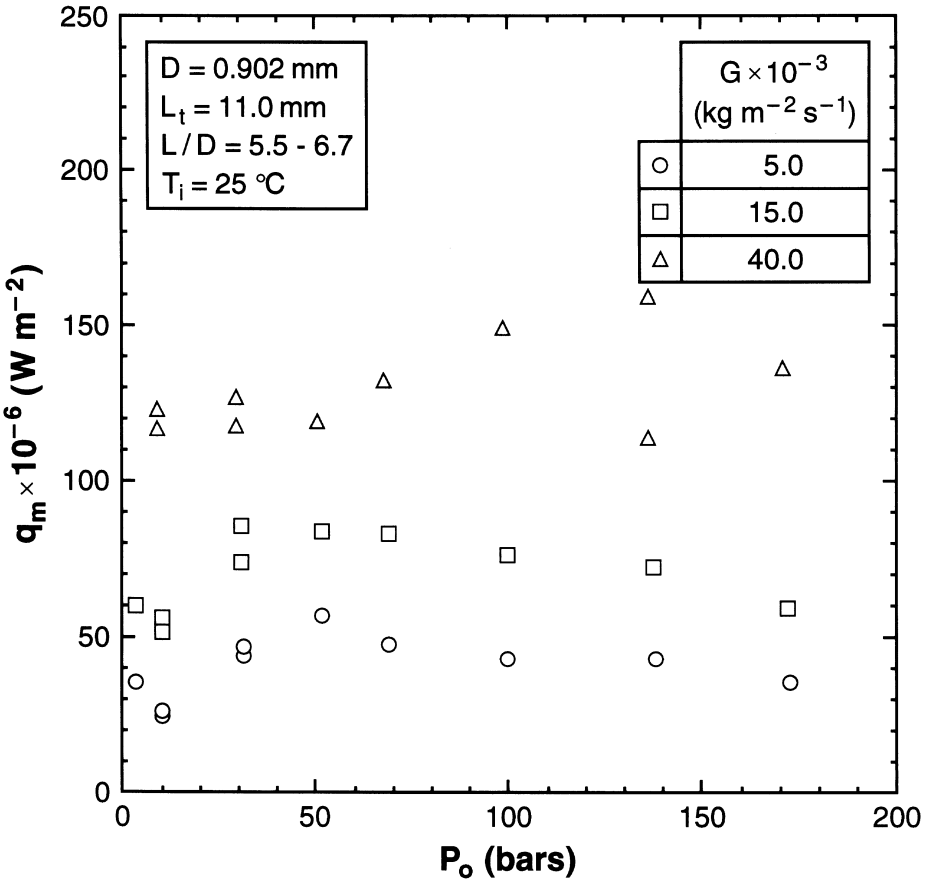

Fig. 14. Effect of outlet pressure on CHF for constant inlet temperature.

from 304 stainless steel and Cu-Ni 30% showed virtually no dependence of ultra-high CHF on tube material.

2. Ultra-high CHF increases with increasing mass velocity, increasing subcooling, decreasing tube diameter, and decreasing heated length-to-diameter ratio. For a constant inlet temperature, CHF increases with increasing pressure for pressures up to 30 bars, remains fairly constant between 30 and 150 bars, and decreases afterwards as critical pressure is approached.
3. Pressure drop for flow boiling at high mass velocity in a short, small diameter tube varies little from the adiabatic single-phase pressure drop, proving CHF is triggered even with negligible net vapor production. Thus, a simple single-phase model seems most suitable for predicting the pressure drop for these conditions.
4. Ultra-high CHF values in excess of 100 MW m^{-2} can be achieved with subcooled water flow at high mass velocities ($G > 40\,000$ kg m^{-2} s^{-1}) in small diameter tubes ($D < 1$ mm) of short heated lengths ($L < 7$ mm). The present study yielded the highest recorded CHF value (276 MW m^{-2}) for flow boiling of water in a uniformly heated tube, surpassing Ornatskii and Vinyarskii's [8] prior record of 228 MW m^{-2}.
5. The highest CHF case discussed above points to upper practical limits on ultra-high heat flux dissipation evidenced by the combination of flow conditions and geometrical parameters. The very high mass velocity ($G = 120\,000$ kg m^{-2} s^{-1}) and small tube diameter ($D = 0.406$ mm) required to achieve this record CHF value resulted in an enormous pressure drop ($\Delta P = 129.3$ bars). Further increases in mass velocity by any significant amount would not be possible because the total pressure drop is limited at the inlet by the critical pressure. In addition, a decrease in tube diameter would also lead to significant increases in total pressure drop. The short heated length of $L = 5.8$ mm helped achieve this record heat flux; however, any further decrease in heated length would be impractical. The use of multiple, short cooling tubes as opposed to one or a few long tubes might be the best cooling scheme to dissipate heat in ultra-high heat flux applications.

Acknowledgement

The authors are grateful for the support of the Office of Basic Energy Sciences of the U.S. Department of Energy (Grant No. DE-FG02-93ER14394.A003).

References

[1] M.B. Bowers, I. Mudawar, High flux boiling in low flow rate, low pressure drop mini-channel and micro-channel heat sinks, International Journal of Heat and Mass Transfer 37 (1994) 321–332.
[2] M.B. Bowers, I. Mudawar, Two-phase electronic cooling using mini-channel and micro-channel heat sinks. Part I. Design criteria and heat diffusion constraints, ASME Journal of Electronic Packaging 116 (1994) 290–297.
[3] M.B. Bowers, I. Mudawar, Two-phase electronic cooling using mini-channel and micro-channel heat sinks. Part II. Flow rate and pressure drop constraints, ASME Journal of Electronic Packaging 116 (1994) 298–305.
[4] R.D. Boyd, Subcooled flow boiling critical heat flux (CHF) and its application to fusion energy components. Part I. A review of fundamentals of CHF and related data base, Fusion Technology 7 (1985) 7–31.
[5] S.S. Kutateladze, A.I. Leont'ev, Some applications of the asymptotic theory of the turbulent boundary layer, Proceedings of the Third International Heat Transfer Conference, Vol. 3, American Institute of Chemical Engineers, New York, 1966, pp. 1–6.
[6] J. Weisman, B.S. Pei, Prediction of critical heat flux in flow boiling at low qualities, International Journal of Heat and Mass Transfer 26 (1983) 1463–1477.
[7] C.H. Lee, I. Mudawar, A mechanistic critical heat flux model for subcooled flow boiling based on local bulk flow conditions, International Journal of Multiphase Flow 14 (1988) 711–728.
[8] A.P. Ornatskii, L.S. Vinyarskii, Heat transfer crisis in a forced flow of underheated water in small-bore tubes, Teplofizika Vysokikh Temperatur 3 (1965) 444–451. High Temperature 3 (1965) 400–406.
[9] G.P. Celata, M. Cumo, A. Mariani, Burnout in highly subcooled water flow boiling in small diameter tubes, International Journal of Heat and Mass Transfer 36 (1993) 1269–1285.
[10] C.L. Vandervort, A.E. Bergles, M.K. Jensen, An experimental study of critical heat flux in very high heat flux subcooled boiling, International Journal of Heat and Mass Transfer 37(Suppl. 1) (1994) 161–173.
[11] R.D. Boyd, Subcooled water flow boiling experiments under uniform high heat flux conditions, Fusion Technology 13 (1988) 131–142.
[12] R.D. Boyd, Subcooled water flow boiling at 1.66 MPa under uniform high heat flux conditions, Fusion Technology 16 (1989) 324–330.
[13] A.E. Bergles, Subcooled burnout in tubes of small diameter, ASME Paper No. 63-WA-182, 1963.
[14] D.D. Hall, I. Mudawar, Ultra-high critical heat flux (CHF) for subcooled water flow boiling—II: high-CHF database and design equations, International Journal of Heat and Mass Transfer 42 (1999) 1429–1456.
[15] M.B. Bowers, High heat-flux dissipation using small diameter channels, Ph.D. Thesis, Purdue University, West Lafayette, IN, 1994.